



Mail Stop 230-5
NASA Ames Research Center
Moffett Field, CA 94035
(415) 694-6363

Research Institute for Advanced Computer Science

SEMI-ANNUAL STATUS REPORT NASA GRANT NCC 2-431

557

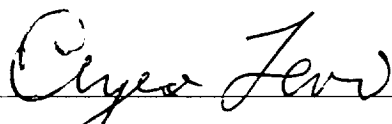
*Submitted in accordance with Section 605
of the NASA Grant and Cooperative Agreement Handbook*

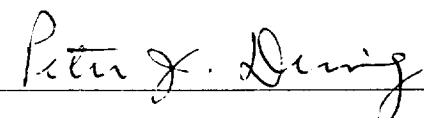
Project Title: Computational Chemistry Research

Technical Monitor: F. Ron Bailey

Principal Investigator: Eugene Levin

For the Period of: January 1987 to July 1987


Dr. Eugene Levin, Principal Investigator


Dr. Peter J. Denning, Director
RIACS
Mail Stop 230-5, NASA
Moffett Field, California 94035
(415) 694-6363

(NASA-CR-196120) COMPUTATIONAL
CHEMISTRY RESEARCH Semiannual
Status Report, Jan. - Jul. 1987
(Research Inst. for Advanced
Computer Science) 53 p

N94-36989

Unclass

G3/25 0014092

inst

STATUS REPORT

Task #41 is composed of two parts: (1) analysis and design studies related to the NAS Extended Operating Configuration (EOC), and (2) Computational Chemistry.

During the first half of 1987, Dr. Levin served as a member of an advanced system planning team to establish the requirements, goals and principal technical characteristics of the NAS EOC. As a result of earlier studies in this area, he presented a paper entitled, "Scaling of Data Communications for an Advanced Supercomputer Network," at the Third International Conference on Data Communications Systems and their Performance, in Rio de Janeiro (June 22-25). The paper was published in the Proceedings of that conference.

A major milestone was reached in a study being conducted by Dr. Levin of RIACS, together with Dr. Partridge and Dr. Stallcop of NASA/Ames. The high temperature transport properties (such as, viscosity, thermal conductivity, etc.) of the major constituents of air (Oxygen, Nitrogen) were correctly determined for the first time. The results of prior ab initio computer solutions of the Schrödinger equation were combined with the best available experimental data, to obtain complete interaction potentials for both neutral and ion-atom collision partners. These potentials were then used in a computer program developed by Dr. Levin to evaluate the collision cross-sections from which the transport properties could be determined. The results are contained in a paper entitled, "High Temperature Transport Properties of Air," by Levin, Partridge and Stallcop, which was presented by Levin at the Twenty-Second AIAA Thermophysics Conference in Honolulu (June 8-10). These results are of importance for the Advanced Orbital Test Vehicle (AOTV) and the National AeroSpace Plane (NASP).

PAPERS PUBLISHED

Eugene Levin, "Scaling of Data Communications for an Advanced Supercomputer Network," Proceedings of the Third International Conference on Data Communications Systems and Their Performance, June 22-25, 1987.

Levin, Partridge and Stallcop, "High Temperature Transport Properties of Air," presented at the Twenty-Second AIAA Thermophysics Conference, June 8-10, 1987.

SCALING OF DATA COMMUNICATIONS FOR AN ADVANCED SUPERCOMPUTER NETWORK

E. Levin*

Research Institute for Advanced Computer Science
NASA Ames Research Center, Mail Stop 230-5
Moffett Field, California 94035, USA

C. K. Eaton and Bruce Young

General Electric Western Systems
4041 N. First St., San Jose, California 95134, USA

The goal of NASA's Numerical Aerodynamic Simulation (NAS) Program is to provide a powerful computational environment for advanced research and development in aeronautics and related disciplines. The present NAS system consists of a Cray 2 supercomputer connected by a data network to a large mass storage system, to sophisticated local graphics workstations and by remote communications to researchers throughout the United States. The program plan is to continue acquiring the most powerful supercomputers as they become available. This paper describes the implications of a projected 20-fold increase in processing power on the data communications requirements.

1. INTRODUCTION

The Numerical Aerodynamic Simulation (NAS) Program was initiated by NASA to establish a national resource for advanced research and development in aeronautics and related disciplines. To achieve this goal the NAS Program is to, "act as the pathfinder in advanced, large-scale computer system capability..." [1,2,3,4]. The first major milestone has been achieved and the initial configuration (Figure 1) is now operational at the NASA Ames Research Center. The centerpiece is a Cray 2 supercomputer with 256 million (64-bit) words of memory and a *sustained* performance rated at 250 MFLOPS (250 Million Floating-point Operations per Second) as measured on benchmark tests for optimized large-scale computational aerodynamic codes.

The need for much more powerful processors can be seen from Figure 2 [1, 2, 3] which depicts the estimated speed and memory requirements for various approximations to the governing equations and three levels of geometric complexity; an airfoil, a wing and a complete aircraft. Note, for example, that if viscosity effects are included by using the Reynolds-averaged Navier-Stokes equations, a three dimensional solution for a wing requires about 100 times the computing speed of a comparable inviscid solution and only now has it become feasible to perform highly repetitive design optimization studies for such cases. Furthermore, if still more realistic large eddy effects are considered, a further factor of about 1000 is required for runs of the same duration. Finally, Figure 2 indicates that (with 1985 algorithms), a single 15 minute run including large eddy effects for a complete aircraft would require computer speed in excess of 10^{12} floating point operations per second and a random access memory of about 10^{11} bytes!

* Work supported in part by Cooperative Agreement NCC 2-387 from National Aeronautics and Space Administration to Universities Space Research Association.

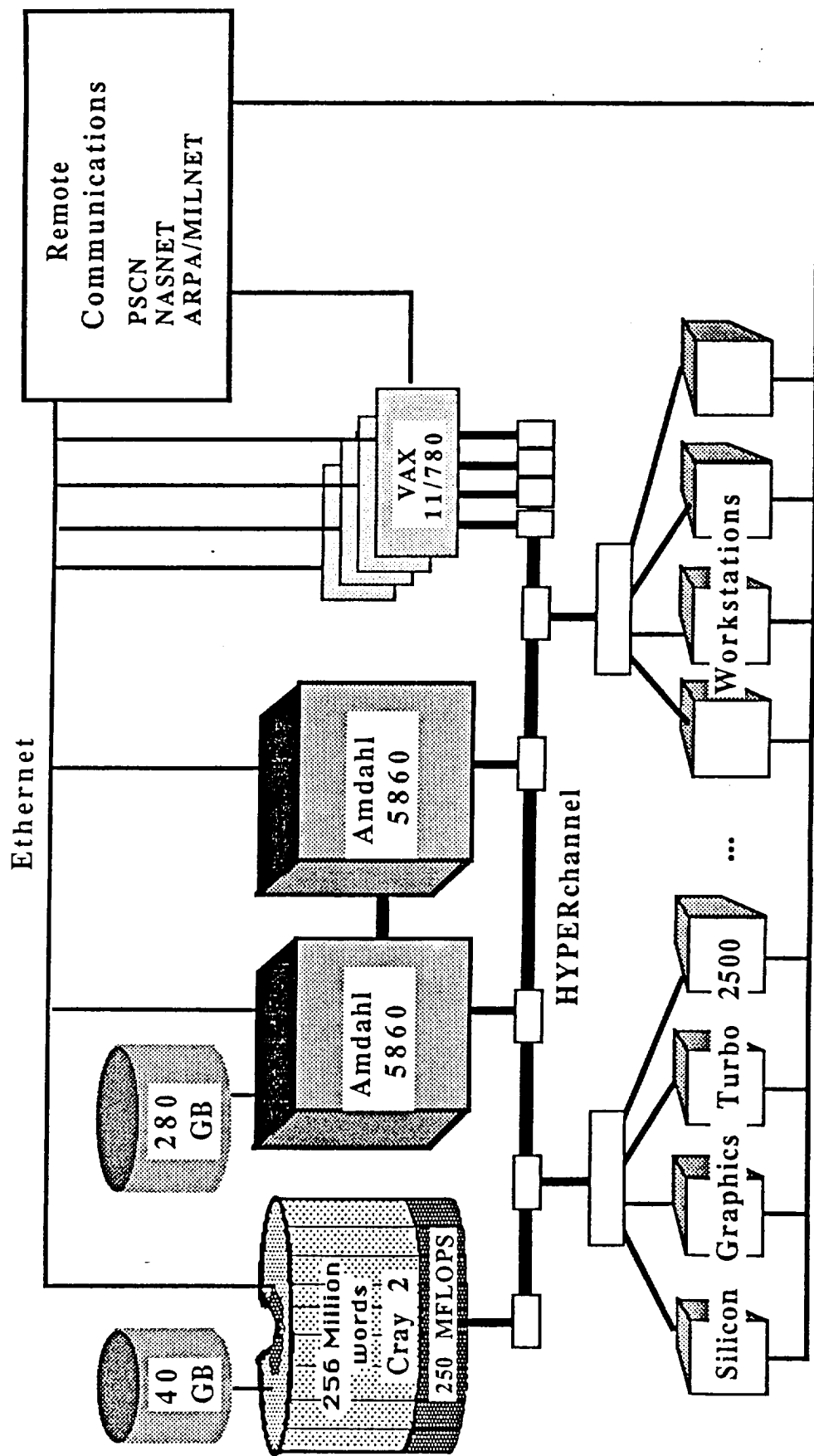


Figure 1. Initial Operating Configuration

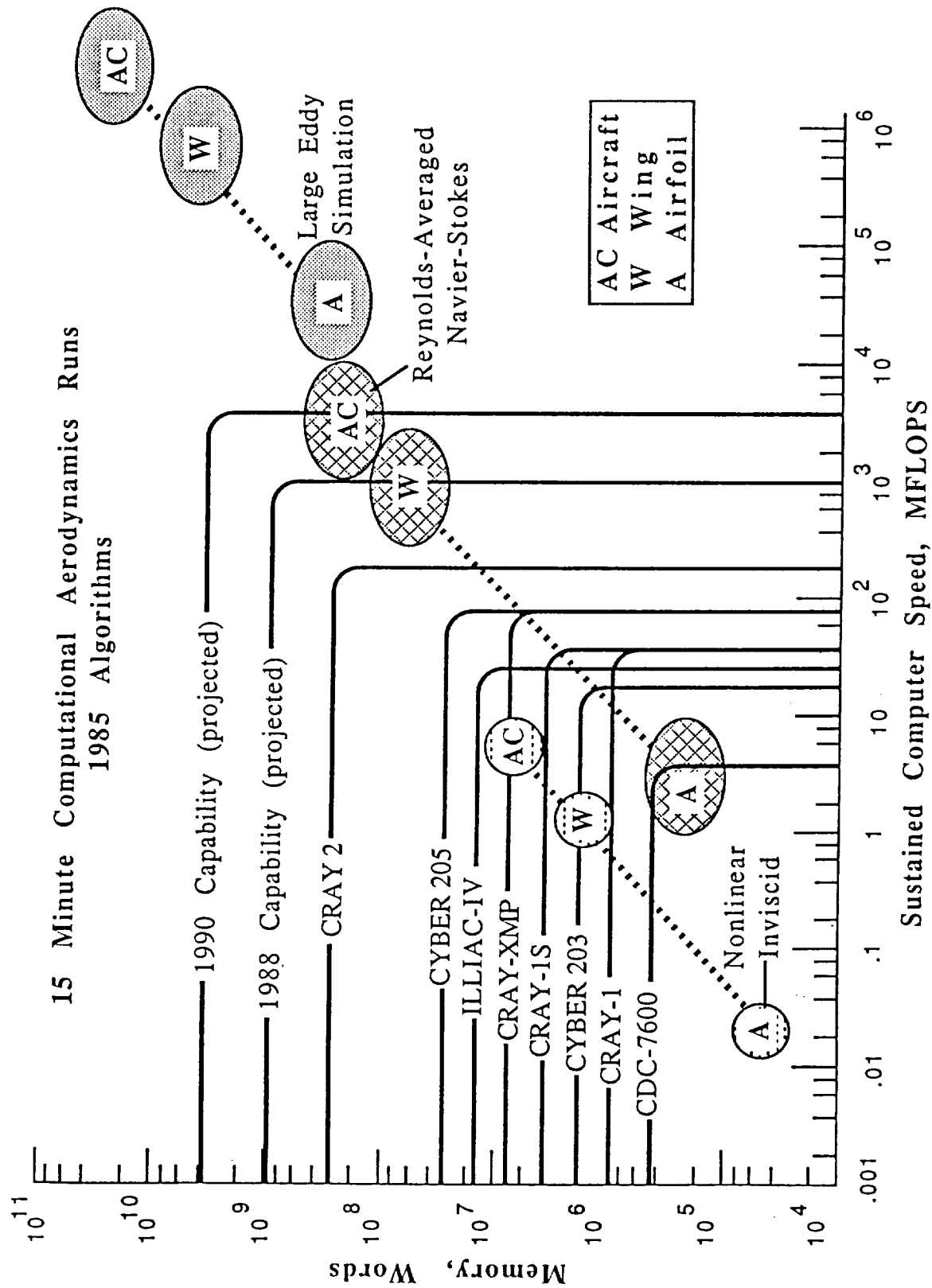


Figure 2. CPU Speed and Memory Requirements

In consideration of these computational needs, the NAS Program plan is to continue to acquire the most powerful supercomputers as they become available. By 1988 it is anticipated that a "one GigaFLOPS" computer with 4 times the *sustained* speed of a Cray 2 will be obtained and by 1990 an additional supercomputer with 16 times the sustained Cray 2 speed (4 GigaFLOPS, i.e., 4000 MFLOPS) will be added. To assure that this increased power can be fully utilized, it is essential to examine the total supporting system-level infrastructure. In particular, it is critical to provide sufficient capacity for the very large data files characteristic of fluid dynamics computations and to scale the bandwidth of the communication systems to handle the increased traffic.

2. RELATED WORK

Several authors have recently considered the "balances" needed between computer speed, storage requirements and data communications. Kung [5] presents a model of balanced computer architectures for particular classes of computation; however his work is primarily concerned with the characteristics of the processor itself and not the total environment. The same limitation is true of "Amdahl's rules of thumb" (see [13]) which Worlton [6] states in the form, "One byte of main memory is required to support each instruction per second," and, "One bit of I/O is required to support each instruction per second."

Thorndyke [7] does consider the support environment for the ETA-10 supercomputer and views the mass storage subsystem as part of a memory hierarchy consisting of central processor memory, shared memory, local disks, and mass storage. He concludes that the capacity ratios between each level of this hierarchy should increase by a factor of 16:1. He also proposes that data communication rates be matched to disk transfer rates of 10 Megabytes/sec. Ewald and Worlton [8] note that the Cray XMP/48 also exhibits a 16:1 ratio between local "disk" storage (Solid State Disk, in this case) and main memory. Furthermore, they note that historically the requirements at all levels of the storage hierarchy have been roughly proportional to the speed of the computer. For future scaling, they propose that on-line disk capacity requirements should grow at about 2/3 of the performance growth of the supercomputer and that transfer rates be increased to achieve a balanced system.

The 1986 work of Wallgren [9] uses similar theoretical scaling laws based on past and current experience to project the supporting environment needed for future supercomputers. His primary focus is on storage and not on data communications requirements. He correctly notes that the results are dependent on the assumed system architecture and on the usage profile. Wallgren's extrapolations extend over more than a decade in time and a factor of as much as 10^4 increase in supercomputer speed.

3. SCOPE

The present study examines the impact on the data communications of a 20-fold increase in computer speed over a 3-4 year time period and specifically assumes an architecture (Figure 3) which is structurally the same as the existing initial operating configuration of Figure 1. Furthermore, the user population is well defined since the NAS Program is not a general purpose scientific computing center but is devoted specifically to aeronautics studies and applications; the program plan calls for some 90% of the total time to be used for computational fluid dynamics and aerodynamics. This permitted a detailed workload model to be developed.

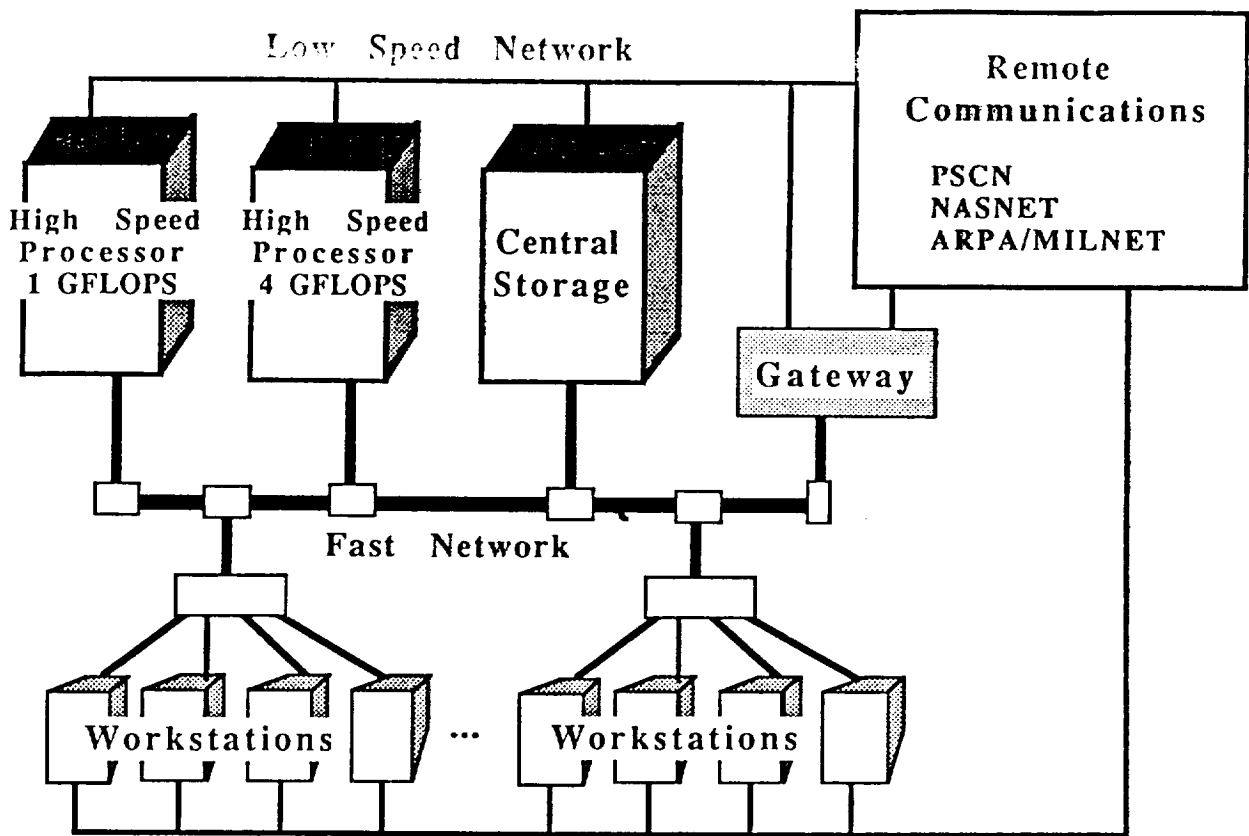


Figure 3. 1990 Model Configuration

4. ANALYSIS OF DATA COMMUNICATIONS

The 1990 system architecture shown in Figure 3 consists of a primary high speed data network between two supercomputers and a central mass storage system; a secondary network for communication between local workstations and the remaining subsystems; and a remote communication subsystem. The primary focus of the study was to determine the requirements for the "backbone" high speed data network for the movement of large files (typically from 5-80 million words) to and from the high speed processors. The remote communication subsystem and the local area network serving the workstations are also scheduled for upgrade, however their sizing was determined by factors *other* than the speed of the supercomputer(s).

4.1. REMOTE COMMUNICATIONS

The NAS remote communications system currently supports Arpanet/Milnet, NFSnet, NASnet, and the NASA-wide Program Support Communication Network (PSCN). Access to the NAS network from remote sites is shown in Figure 4. Vitalink bridges manage the inter-network connection and monitor all traffic on the ethernet local area network passing only those messages that have remote destination addresses to the appropriate Vitalink unit.

Both terrestrial links (at 56 and 244 Kilobits/sec) as well as satellite T1 links (at 1.544 megabits/sec to the NASA centers) are provided. At present, over 20 remote sites (with approximately 100 users) have been activated and additional sites will be added to expand the user community.

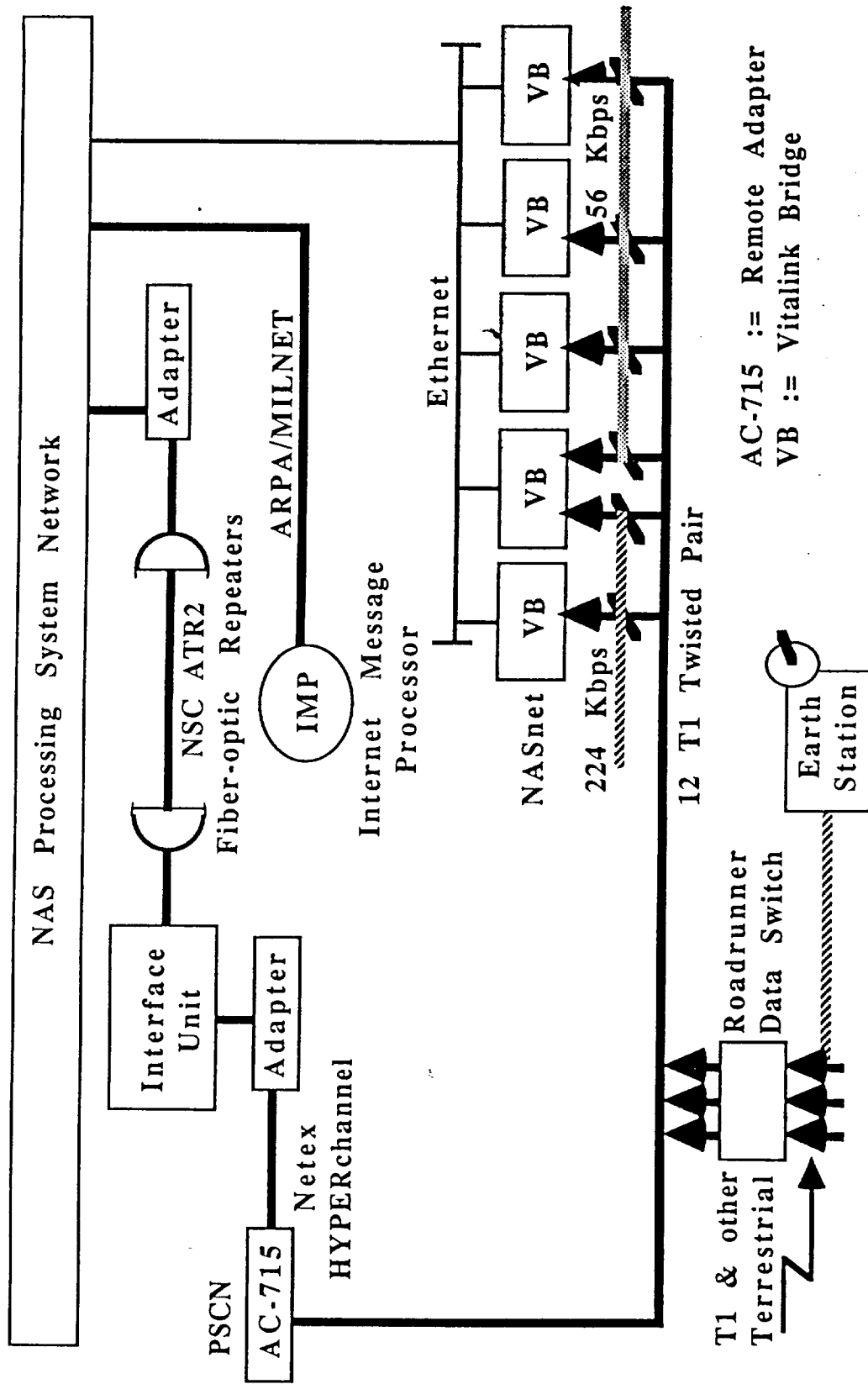


Figure 4. NAS Remote Communications

The long term goal is to provide equivalent services to both local and remote NAS users. This objective is constrained by technology and funding limitations. Upgrade to T2 rates (6.2 megabits/sec) for selected NASA centers is planned during the 1988/1989 time period. Additional improvements under investigation include implementing class of service protocols (such as distinguishing bulk file transfers from interactive traffic) and techniques for reducing the volume of remote data communications (such as remote block editors and distributed graphics services).

4.2 LOCAL WORKSTATION COMMUNICATIONS

The principal local users access the NAS system through powerful graphics workstations (Silicon Graphics 2500 Turbos). The workstation is an essential element of the system to permit graphical analysis and interpretation of the extremely large output files generated by computational fluid dynamics batch programs. It also enables the user to work interactively with the supercomputer. For example, a user may designate locations in the vicinity of an aerodynamic surface on his display, the flow patterns representing particle traces from those locations are computed on the supercomputer and the results returned to the user's display. The data communications services to the workstation must be sufficient to enable the user to make maximum use of both the batch and interactive workstation/supercomputer capabilities.

There are three modes in which graphics can be displayed at the workstation. It is possible to send down the solution files (or large subsets of these files) for computation and display at the local workstation. Although the workstation has the processing power comparable to a Vax 11/780 and the special purpose graphics hardware expedites the generation and transformation of vectors and polygons, there are many limitations to this mode of operation including the I/O bandwidth of the workstation and limitations of main memory and disk space. The preferred modes use the supercomputer for the computationally intensive tasks and send down either display lists or pixel data to the workstation. Both modes may be used, however with the current workstations it is difficult to use the pixel mode of interaction effectively. Future workstation upgrades will alleviate this limitation and the 1990 model assumes that both the display list mode and the pixel mode of interaction will be used extensively.

Based on the above description of operational use, the data communications requirements to the workstation are primarily sized according to the graphics needs of the user and the projected capabilities of future workstations. The present *effective* rate of approximately 2 Megabits per second is appropriate for the current workstation receiving display lists (typically 2.6 Megabits in size) from the supercomputer since the transmission time (1.3 seconds at 2 Megabits per second) is only a fraction of the time needed for the workstation to generate the display (approximately 5 seconds). Some representative display capabilities at 8 Megabits per second (the minimum planned for 1990) are shown in Table 1. For example, a *minimal* pixel file of 8 Megabits (display resolution of 1,000 x 1,000 with 8 bits/pixel for simple color and shading) can be transmitted in 1 second and the time for the workstation to generate a display from such a file is negligible. A very high quality pixel file of 96 Megabits would require 12 seconds of transmission time but this would typically be used for presentation quality graphics only. (For comparison, the data rate needed to support real time, interactive, color graphics with animation at 30 frames/sec. would be about 800 megabits/sec. The NAS Program is funding a prototype of such a bus and considering prototyping an advanced graphics workstation with a massive frame buffer and very high resolution, however this is not included in the 1990 system model.)

Table 1. Display of Color Images

Type of Output from Supercomputer to Workstation	Typical File Size	Channel Time @ 8 Mbps	Time for Workstation to Generate Display
Current Workstation (8000 Polygons, includes Hidden Surface Removal, Flat Shading)			
Solution File	400 Megabits (near storage limit)	30 seconds	≈ 25 seconds
Display List	2.6 Megabits	0.3 seconds	≈ 5 seconds (≈ 1 second if no hidden surface removal)
Future Workstation			
Minimal Pixel File	8 Megabits (1k x 1k x 8 bits)	1 second	<< 1 second
Fully Rendered, Very High Quality, Pixel File	96 Megabits (2k x 2k pixels 24 bits/pixel)	12 seconds	<< 1 second

4.3. HIGH SPEED "BACKBONE" COMMUNICATIONS

The high speed data communication requirements were derived by analysis of a model of the expected workload and checked using a discrete simulation program. The workload model assumed that the processing power of 5 Gigafllops available from the two 1990 high speed supercomputers (Figure 3) was fully utilized. A detailed profile (for computational fluid dynamics) of types of user tasks and expected frequencies had been developed over a six year time period and was updated in 1986 to reflect current algorithms, projected increased interactive usage and substantially increased use of graphics [10, 11, 12].

The model contained over two hundred parameters including: numbers and types of local and remote users, number of host processors, protocol delays, amount of disk storage attached to the supercomputers, distribution of batch and interactive work, frequency of task execution, probability of abortive runs, etc. Scripts were developed to represent characteristic delays associated with "think time" to separate user-initiated sequential processes. These asynchronous processes compete for system resources. The high speed data communications capability was initially taken as unbounded and the workload was progressively increased until the full capability of the supercomputers was saturated.

A simplified listing of the classes of work initiated by the users is summarized in Table 2. The principal execution runs represent various types of numerical aerodynamic simulations used to solve fluid flow problems. These generally involved repeated iterations of

difference equations over a three-dimensional grid which was assumed to consist of one million grid points. The simple steady state design simulations used an inviscid potential and required approximately 20,000 calculations per grid point of result file. The more complex steady state design simulations used the Reynolds-Averaged form of the Navier-Stokes equations and required approximately 600,000 calculations per grid point. The comparable unsteady solutions typically required over 4 million computations per grid point. The "model day" included 73 hour-long runs of this computation, each requiring 1.0 GigaFLOPS of sustained processing power. From Table 2 it is evident that this represented the dominant load on the supercomputers.

Table 2. Estimated Processor Load of User Initiated Runs

<u>TASK</u>	<u>GFLOP/DAY</u>
CODE & PARAMETER PREPARATION	66
PATCH GENERATION	43
GRID GENERATION	96
METHOD AND CODE DEVELOPMENT	13,003
SIMPLE STEADY STATE DESIGN SIMULATIONS	5,732
COMPLEX STEADY STATE DESIGN SIMULATIONS	31,834
COMPLEX UNSTEADY STATE DESIGN SIMULATIONS	250,978
FLUID RESEARCH LARGE EDDY SIMULATIONS	53,472
RESULT EDITING & VIEWING	17,465
DOCUMENT PREPARATION & USER COMMUNICATIONS	31
<u>TOTAL</u>	<u>372,719</u>

In order to relate the computational loads to network traffic, a Workload Data Base was constructed which contained detailed estimates of the sizes of the various input/output files *for each task* and a model of how they would be utilized. This provided a means for determining the specific files generated and their movement across the network. For example, Table 3 shows the network traffic load for the dominant Unsteady Design Simulation task.

Table 3. Network Load for Unsteady Design Simulations
MB/day

<div>Sources Destinations</div>	MASS STORAGE	HIGH SPEED PROCESSORS	TOTAL
MASS STORAGE	-	4,428	4,428
LONG-HAUL COMMUNICATIONS	0.2	2,048	2,048
WORK- STATIONS	0.1	1,810	1,810
HIGH SPEED PROCESSORS	1,555	-	1,555
TOTAL	1,555	8,286	9,841

The source of most of the data communications load comes from the output of large files from the the high speed processors to their local disks and the subsequent movement of these files between the supercomputers and the central mass storage system. Figure 5 shows the results of the model study for this traffic. There is a predicted net accumulation on the local disks of 42 Gigabytes per day which must be moved (by system-managed file migration) to the central mass storage system so that the supercomputers' disk space will be available for current work. The two supercomputers of the 1990 system were modelled with a total of 400 Gigabytes of local storage. Since more than half the available 400 Gigabytes is needed for current working space each day, the average age of files before automatic migration to central storage was found to be about 3.5 days. This additional load (of automatic migration) on the data communications can, however, be distributed over the periods of lightest user activity. Typically the nighttime workload consists of large batch jobs with little interactive traffic. Under these conditions the supercomputers are fully saturated but the network is only lightly loaded.

**Note: Supercomputer Disks
Daily Net Accumulation = 42 GB**

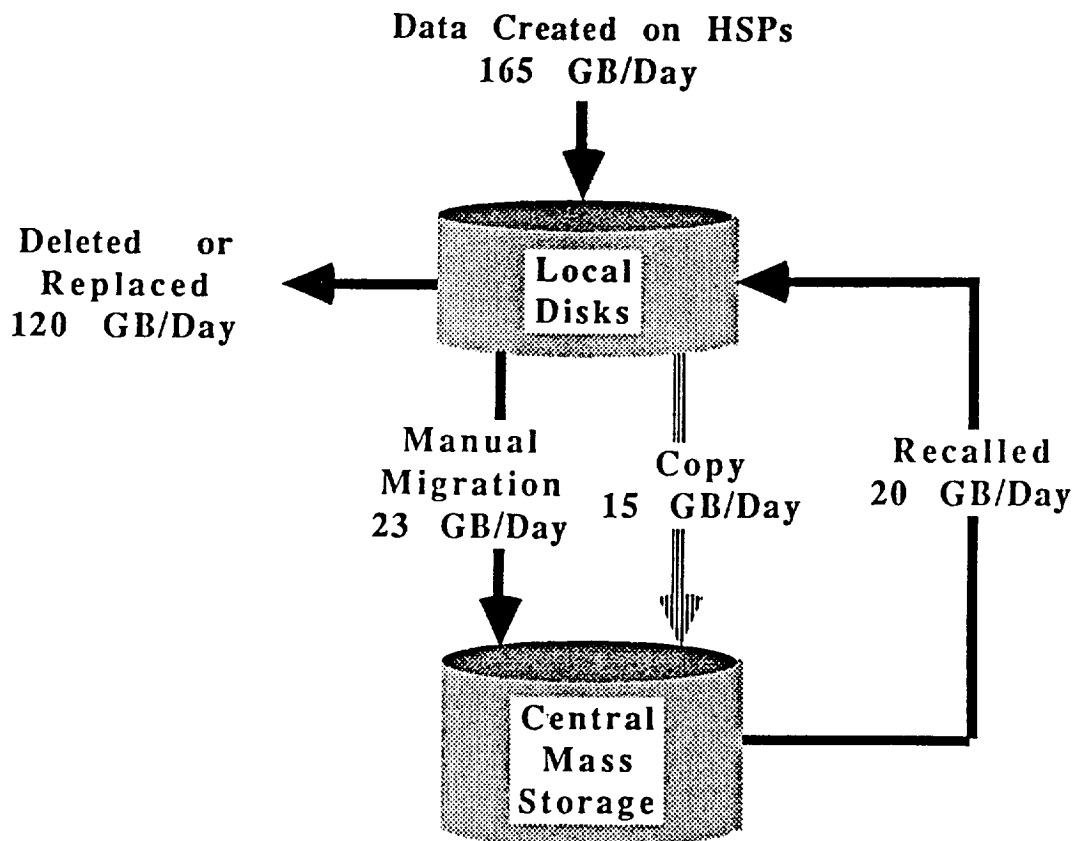


Figure 5. Daily File Activity

Figure 6 summarizes the major result of the study and illustrates both the hourly distribution of traffic as well as the average daily traffic including migration. To avoid significant queuing delays during times of peak activity, and to handle periodic bursts within an hour efficiently, the bandwidth for the 1990 system should be sized well in excess of the peak rates shown on Figure 6. The design value recommended was 100 megabits per second [14]. This was regarded as a reasonable requirement in view of projected technological advances.

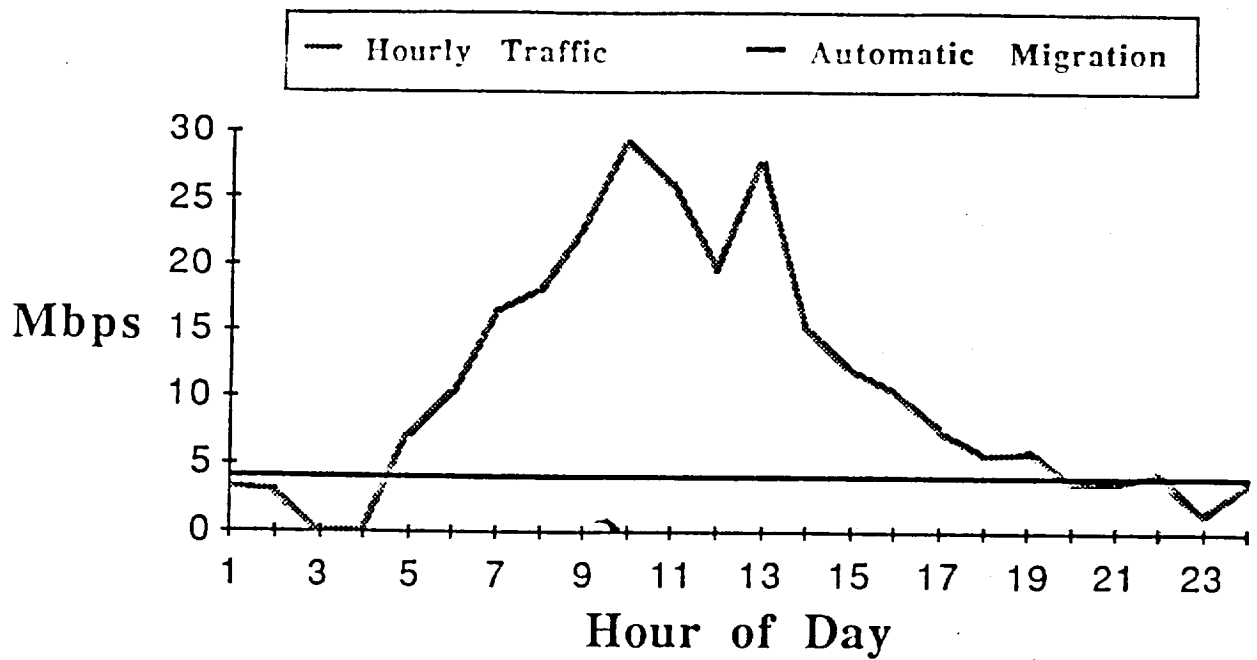


Figure 6. Data Transfer Rates

5. CRITIQUE OF RESULTS

An essential (but often neglected) step in studies of this type is to estimate the sensitivity of the results to the assumptions inherent in the model. The succeeding sections provide estimates of the effects of some of the major assumptions on the projected data communications requirement.

5.1. USE OF GRAPHICS

The need for sophisticated graphics to analyze the very large data files typical of computational fluid dynamics is unquestioned and a significant allowance for this type of processing was included in the model. However, this was a projection and might not correspond to the actual future usage. Among other factors it is dependent on the capabilities of future workstations.

The model provided a breakdown into various types of output. The three principal classes created were raw solution results, graphics display lists and pixel files. It was found that a very useful measure for scaling data communications with processing power was the ratio of bytes of output to MFLOPs (millions of floating point operations) required to generate that output. This *characteristic output ratio* will be designated β_M with units of Bytes/MFLOP. The importance of this parameter is that if the *only* deviation from the assumed model is processing power, the results can (within reasonable limits) be scaled directly. Furthermore, if the mix of classes of output varies, it is possible to estimate the effect on this critical parameter and hence (within modest bounds) on the final results.

Over the distribution and frequency of tasks initiated by users, the model showed that raw result files (including debug runs) were found to generate $\beta_M = 130$ B/M (Bytes per MFLOP). In contrast, the generation of graphics display lists generate $\beta_M \approx 8,000$ B/M and pixel files generate $\beta_M \approx 5000$ B/M. In the model, 5% of the total available processing power (FLOPs) was devoted to graphics. Approximately 75% of the graphics

FLOPs were utilized for pixel files, however much more processing is required for pixel files. Hence, this distribution corresponded to approximately three graphics display lists for each pixel file produced. Since the supercomputer power of the 1990 model system was sized at 5 GFLOPS, the 5% utilized for graphics corresponds to 250 MFLOPS, equivalent to the total sustained processing capability of the 4 CPU's of a CRAY 2!

For the assumed usage distribution, the overall value of the characteristic output ratio for the 1990 model was found to be $\beta_M \approx 400$ Bytes/Mflop. Figure 7 shows the variation in this parameter with changes in the relative amount and type of graphics usage. The abscissa represents the proportion of processing power used for graphics processing (both display list and pixel data) and the one-parameter family of lines represents various mixes of pixel output and display list output. The reference point corresponding to the model is marked. As an example, the calculation of the design point (using the data values of the paragraph above) is shown below:

$$0.95(130) + 0.05[0.75(5000) + 0.25(8000)] = 411 \text{ Bytes/Mflop.}$$

It may be noted that increased use of pixel data relative to display list output has a significant effect in reducing β_M . Display list output with a β_M of 8,000 B/M (compared with pixel file output with a β_M of 5000) utilizes less supercomputer processing power but places a greater load on the data communications (and on the workstations).

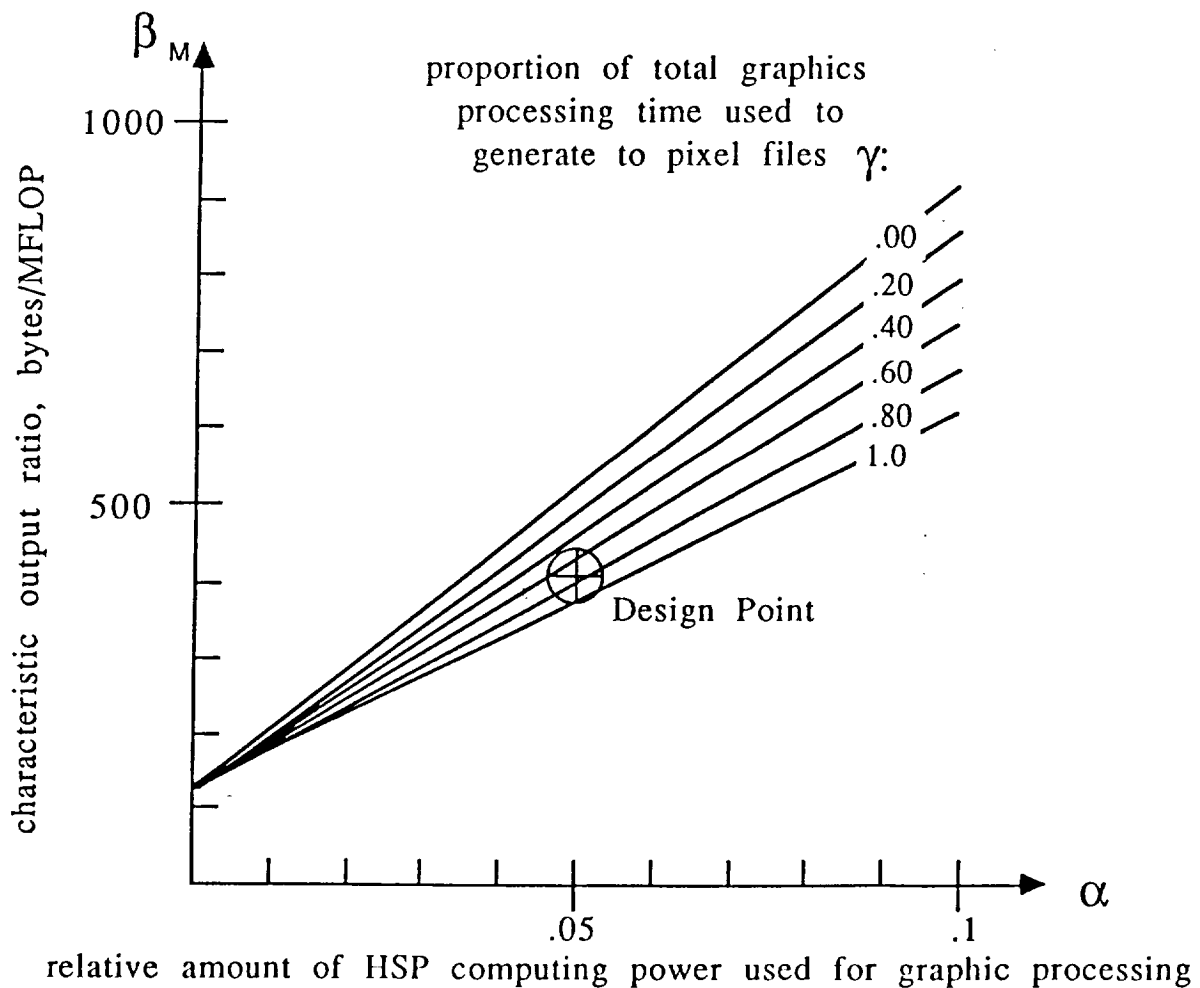


Figure 7. Influence of graphics processing

5.2. THE USER PROFILE

The workload model was specifically designed for solving problems in computational fluid dynamics. Table 4 summarizes a 1986 study of major users of supercomputers at the NASA Ames Research Center. The first two columns represent supercomputers of the Ames Central Computing Facility and only the Cray 2 is a NAS supercomputer. Furthermore, the sampling period shown in Table 4 occurred shortly after the Cray 2 was initially installed, in a pre-operational time period, and does not represent the *intended* operational distribution of users. Nevertheless, it appeared that computational chemistry utilized large amounts of supercomputer time and might represent a future NAS system user that was not reflected in the workload model.

Table 4. Ames Vector Processor Utilization
Percentage of User Time by Organization

USERS	CYBER 205 FY 85	CRAY X-MP 48 3/86-10/86	CRAY 2 3/86-10/86
Remote	-----	-----	36.8 %
Advanced Aerodynamics Concepts	-----	7.1 %	-----
Applied Computational Fluids	0.1 %	24.1 %	7.0 %
Experimental Fluid Dynamics	0.7 %	6.1 %	-----
Computational Fluid Dynamics	25.0 %	24.1 %	13.8 %
Computational Chemistry	67.9 %	16.0 %	19.2 %
TOTAL	93.7 %	77.4 %	76.8 %

Much of the current work in computational chemistry at NASA Ames Research Center is devoted to determining the electron density distribution of molecular structures by solving the Schroedinger equation. The methods used involve evaluation of many multi-dimensional integrals and manipulation of very large matrices to find eigenvectors and eigenvalues. These methods are quite different than those used in computational aerodynamics studies. Hence the output of such runs might produce larger or smaller files than those used in the model.

Consequently, a study was made of the character of the output files generated by these supercomputer users. The results are shown in Figure 8 in terms of the parameter β_M . The prediction of the 1990 model study is shown for comparison. The characteristic output of computational chemistry was found to be comparable to the major computational aerodynamics users. Hence, even if computational chemistry were in the future to become a significant component in the mix of NAS users, it was concluded that this would not invalidate the results.

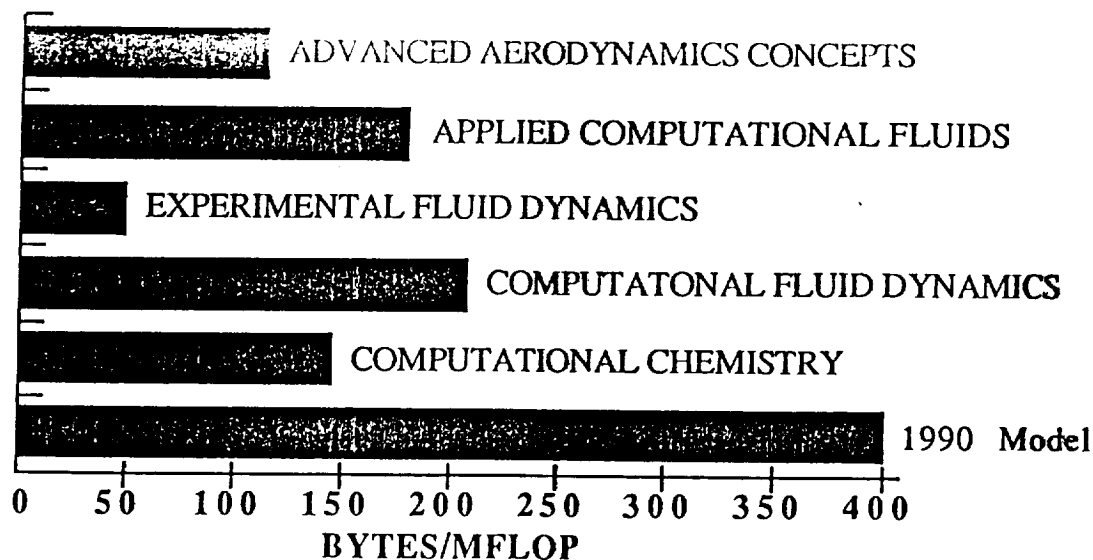


Figure 8. Comparison of Current Usage and 1990 Model

It is also of considerable interest to note the relationship of the predicted 1990 usage compared to actual 1986 usage. It is not surprising that the predicted value of β_M (≈ 400 Bytes/MFLOP) is almost twice the 1986 measured values in Figure 8 since extensive use of graphics was just beginning. Figure 7 confirms that increased graphics use results in an increase in β_M .

5.3. AMOUNT OF LOCAL DISK STORAGE

Locality of files increases the hit rate and reduces the volume of data traffic (see [15]). If local storage were unlimited, there would be no need to move files to a central storage facility. If files could be maintained local to the supercomputers for about 10 days (two working weeks) instead of 3.5 days, it was estimated that the recall load would be reduced from 20 Gigabytes per day to less than 10 Gigabytes per day. Aging would also increase the number of files deleted and decrease the amount of manual migration shown in Figure 5. All of these effects decrease the traffic on the network. It was estimated that increasing the local disk storage by an additional 250 Gigabytes could reduce the traffic between the supercomputers and central storage by 30-50%.

5.4. OTHER CONSIDERATIONS

The model assumed a typical grid size of 10^6 points. Increasing the geometrical refinement by using more grid points does not have any affect on β_M provided the computations needed per grid point remain constant. However, in many cases not all the final data needs to be saved. The finer grid not only yields results at more spatial locations but also permits a more accurate approximation to the differential equation. It is often only necessary to save the results on a much coarser grid (except for critical regions of interest) and recompute the interior points if needed. For example, saving every fourth grid point in each dimension would reduce the output by a factor of 64. Similarly, it may not always be necessary to save 64-bits of precision in the output data.

The realism of the physics was discussed briefly in connection with Figure 2 where it was noted that solving the more complex equations such as large eddy simulation involved an enormous increase in the number of computations. There would certainly not be a proportionate increase in the output, hence the trend towards removing the approximations would result in a sharp decrease in the ratio β_M and alleviate the data communications load. This was a factor in the 1990 model and will become increasingly significant as more powerful supercomputers become available.

It was assumed that the algorithms used in the 1990 time frame would be the same as those presently known or in use. This is quite unlikely since algorithm development is a fertile, on-going activity. Prior trends have been in the direction of progressively decreasing β_M , but it is impossible to predict the implications of undiscovered algorithms. If there is a *radical* change from deterministic approaches to statistical techniques (for example, gas lattice automata methods, [16]) this would clearly require much more computational effort without a corresponding increase in output, resulting in a sharp decrease in β_M .

6. SUMMARY

The results of an analysis of the 1990 "backbone" data communications requirements for the advanced Numerical Aerodynamic Simulation Program showed that the expected workload required an *effective* bandwidth of 100 megabits per second.

A critical examination of the various assumptions inherent in the model indicated that 100 Mbps was a safe, conservative result.

Among the most sensitive assumptions was the projected amount and type of interactive graphics expected to be used.

Increasing the amount of disk storage local to the supercomputers would result in a significant decrease in the data communications requirements.

The characteristic output ratio β_M (representing a measure of bytes of output relative to megaFLOPs of processing) made it possible to estimate the effects of (modest) variations in the model assumptions on the data communications requirements.

ACKNOWLEDGEMENTS

The authors wish to express their appreciation to Mr. Frank Preston of the NAS Systems Division, NASA Ames Research Center and Mr. Ari Ollikainen of General Electric Western Systems for useful data and valuable suggestions during the preparation of this paper.

REFERENCES

- [1] Peterson, V.L., Ballhaus, W.F., Jr., and Bailey, F.R., "Numerical Aerodynamic Simulation (NAS)", *Large Scale Scientific Computation*, ed. by Seymour V. Parter, Academic Press, Inc., 1984
- [2] Bailey, F.R. and Ballhaus, W.F., "A Large Scale Computer Facility for Computational Aerodynamics", *IEEE Transactions on Nuclear Science*, Vol. NS-32, No. 1, 1985.
- [3] Bailey, F.R., "Status and Projections of the NAS Program", Symposium on Future Directions of Computational Mechanics, ASME Annual Meeting, Anaheim, CA., Dec. 1986 (Also available as NASA Technical Memorandum 88339, July 1986)
- [4] "Numerical Aerodynamic Simulation Program NPSN System Specification for IOC", NASA Ames document PS-1100-01-C00, 27 February 1984
- [5] Kung, H.T., "Balanced Computer Architectures", *J. Complexity*, V. 1, 1985 (Also available as "Memory Requirements for Balanced Computer Architectures", Carnegie-Mellon University, CMU-CS-85-158)
- [6] Worlton, J., "Some Notes on Storage Systems for Supercomputers", Presentation at Los Alamos National Labs., June 1985
- [7] Thorndyke, L.M., "Supercomputers and Mass Storage: The Challenges and Impacts", *IEEE Symposium on Mass Storage Systems*, Tucson, Arizona, Nov. 1985
- [8] Ewald, R.H., and Worlton, W.J., "A Review of Supercomputer Installation Mass Storage Requirements", *IEEE Symposium on Mass Storage Systems*, Tucson, Arizona, Nov. 1985
- [9] Wallgren, K., "Supercomputing and Storage", *SPIE 30th Annual International Symposium*, August 1986, San Diego, Ca.
- [10] "NPS System Specification, Appendix II, Multi-Task Model", NASA Ames document PC-320-02, 15 September 1980
- [11] "Revisions to Multi-Task Model for NAS Program", NASA Ames document PD-1000-01-C00, 6 February 1984
- [12] "Workload Data Base Overview", NASA Ames document PR-1101-00-N00, 18 February 1986
- [13] Sieworeck, D.P., Bell, C.G. and Newell, A., *Computer Structures: Principles and Examples*, McGraw Hill, New York, 1982
- [14] "Numerical Aerodynamic Simulation Program NPSN System Specification for the Extended Operating Configuration", NASA Ames document PS-1101-01-C00, 13 September 1986
- [15] Smith, A.J., "Long Term File Migration: Development and Evaluation of Algorithms", *Communications of the ACM*, V. 24, No. 8., August 1981
- [16] Frisch, U., Hasslacher, B., and Pomeau, Y., "Lattice Gas Automata for the Navier-Stokes Equation", *Phys. Rev. Lett.*, 56(1986) 1505

HIGH TEMPERATURE TRANSPORT PROPERTIES OF AIR

E. Levin*

Research Institute for Advanced Computer Science
NASA Ames Research Center, Moffett Field, California

Harry Partridge and J. R. Stallcop
Computational Chemistry Branch, Thermosciences Division
NASA Ames Research Center, Moffett Field, California

ABSTRACT

We have developed a general computer code to allow calculation of atom-atom and ion-atom transport collision integrals from accurate potential energy curves described by a set of discrete data points (e.g., RKR turning points and energies derived from molecular structure computations) for a broad range of scattering conditions. This code is based upon semiclassical approximations that properly account for quantum mechanical behavior such as tunneling effects near a barrier maximum, resonance charge exchange, and nuclear symmetry effects. We have determined transport collision integrals for N-N, O-O, N⁺-N, and O⁺-O interactions from complete sets of accurate potential functions derived from combined experimental and *ab initio* structure calculations. For the O-O case, this includes results for excited states; i.e., all possible collisions involving O(³P), O(¹D), and O(¹S). Our calculated values of the N⁺-N and O⁺-O resonance charge exchange cross section Q_{ex} agree well with measurements from beam experiment that are available at high energies where the diffusion cross section Q_d satisfies $Q_d \approx 2Q_{ex}$. Tables of collision integrals and plots of viscosity, thermal conductivity, and diffusion coefficients that are needed to determine the transport properties of high temperature air are presented.

* Work supported in part by Cooperative Agreement NCC 2-387 from the National Aeronautics and Space Administration (NASA) to the Universities Space Research Association (USRA).

I. INTRODUCTION

Transport properties involving high temperature air are of increasing importance. In particular, they are needed for a real gas analysis of the nonequilibrium shock layer flows about Aeroassisted Orbital Transfer Vehicles (AOTV's) during their aerobraking maneuvers at high altitudes in the earth's atmosphere and for design studies of the National Aerospace Plane (NASP).

The determination of transport properties requires knowledge of the potential energy curves for the various interacting species. Existing calculations have, by and large, been based on incomplete potential information; i.e., generally only the RKR (Rydberg-Klein-Rees) curves near the well minimum for a few bound states and often meager potential data on the higher lying molecular states. Furthermore, the method of calculation of the transport properties was based upon fitting the potential data by adjusting the parameters of an assumed analytical form (e.g., Morse potential). Such analytical forms fail to exhibit the correct long-range interaction potential. These various omissions and approximations limit the reliability of previously computed transport properties.

The present work incorporates three major improvements: accurate representation of the interaction curves for a very large set of interacting atomic and ionic species, use of spline curves to fit the available potential data with no *a priori* constraints as to the functional form, and incorporation of certain quantum effects. We have carefully combined the available experimental data with interaction energies obtained from *ab initio* structure calculations to construct the best representation of all the potential curves for O-O, N-N, N^+-N , and O^+-O when the collision partners are in their ground states. In addition, we have included the excited states of O-O to allow the assessment of their contribution to transport properties under nonequilibrium conditions. In all cases the long-range interactions were also correctly represented to cover the entire range of separations necessary for the accurate calculation of transport properties.

The potential data was constructed from complete sets of accurate *ab initio* calculations. For example, our computed potential curves for N^+-N , and O^+-O interactions [1] agree to within 0.2 eV with the RKR curves in the region of the potential minimum. Our calculated long range potential energies have been applied to determine resonance charge exchange cross sections [2] that agree well with the N^+-N , and O^+-O cross sections measured by beam experiments. In the case of N^+-N interactions we have found that potentials which were previously thought to be entirely repulsive, were instead, in fact, bound [3], and hence could affect the predicted transport properties. Our calculation of complete sets of accurate ion-atom potential energy curves for the N^+-N , and O^+-O interactions permits the determination of reliable transport properties for these species for the first time.

A second feature of the present work is the use of our new computer code, "SKATR" that enables the calculation of collision integrals for a broad range of scattering conditions from the actual potential energy as specified by a discrete set of data points, rather than approximate analytical fits. The program is structured to fit a spline curve through the discrete data and subsequently to join smoothly with a correct

specification of the long-range interaction. The program also incorporates the quantum mechanical effects of the semiclassical formulation described below.

We have replaced the non-physical singularity of the classical deflection function at the potential energy barrier maximum by a uniform phase shift approximation due to Stallcop [4], which includes the quantum effects of barrier tunneling and resonance scattering arising from the metastable energy levels of the inner well. Other quantum mechanical behaviour taken into account by our approach includes resonance charge exchange, which dominates the like ion-atom diffusion process at high energies, and nuclear symmetry effects which are significant at low energies. Application of the semiclassical approximation should yield accurate cross sections even at low collision energies. This prepares a foundation for future studies involving very light collision partners such as hydrogen (important for the propulsion system of the NASP). Furthermore, the semiclassical approach allows us to calibrate the accuracy of the classical method (which requires much less computation) and to ascertain its range of applicability.

The mathematical formulation including the semiclassical approximation is described in Section II. In Section III, we present the details of the construction of the accurate interaction curves used as input. A brief description of the SKATR program is presented in Section IV. The calculated results are shown and discussed in Section V, followed by concluding remarks and observations in Section VI.

II. METHOD

According to Chapman-Enskog theory [5], the transport properties of a dilute gas can be expressed in terms of the transport collision integrals,

$$\sigma^2 \overline{\Omega}_{n,s}(T) = F(n,s) \int_0^\infty e^{-x^2} x^{2s+3} Q_n(kTx^2) dx, \quad (1)$$

$$\text{where } F(n,s) = \frac{4(n+1)}{\pi(s+1)! [2n+1 - (-1)^n]},$$

k is the Boltzmann constant, T is the temperature, σ is the hard sphere collision diameter, and $\sigma^2 \overline{\Omega}$ is the mean collision integral.

For a gas mixture to first order, or a pure gas to second order, the transport collision integrals required are: $\sigma^2 \overline{\Omega}_{1,1}$, $\sigma^2 \overline{\Omega}_{1,2}$, $\sigma^2 \overline{\Omega}_{1,3}$, $\sigma^2 \overline{\Omega}_{1,4}$, $\sigma^2 \overline{\Omega}_{1,5}$, $\sigma^2 \overline{\Omega}_{2,2}$, $\sigma^2 \overline{\Omega}_{2,3}$, $\sigma^2 \overline{\Omega}_{2,4}$, and $\sigma^2 \overline{\Omega}_{3,3}$ [6].

For example, for a pure gas to first order,

$$\text{Viscosity: } \eta = 2.6693 \times 10^{-5} \frac{(MT)^{\frac{1}{2}}}{\sigma^2 \overline{\Omega}_{2,2}(T)}, \text{ g cm}^{-1} \text{ sec}^{-1}$$

Thermal Conductivity: $\lambda = 0.19891 \frac{(T/M)^{1/2}}{\sigma^2 \bar{\Omega}_{2,2}(T)}$, mcal cm⁻¹ sec⁻¹ K⁻¹

Self-diffusion Coefficient: $D = 2.628 \times 10^{-3} \frac{(T^3/M)^{1/2}}{p \sigma^2 \bar{\Omega}_{1,1}(T)}$, cm² sec⁻¹

where M is the molecular weight in g/mole, $\sigma^2 \bar{\Omega}$ is in square Angstroms, T is the Kelvin temperature, and p is the pressure in atmospheres.

For a gas mixture, the corresponding diffusion coefficient becomes

Binary Diffusion Coefficient: $D_{ij} = 2.628 \times 10^{-3} \frac{(T^3/2\mu)^{1/2}}{p \sigma^2 \bar{\Omega}_{1,1}(T)}$, cm² sec⁻¹

where $\mu = \frac{M_i M_j}{M_i + M_j}$.

The pure gas viscosities, thermal conductivities, and diffusion coefficients can be used together with the binary diffusion coefficient and species concentrations to determine the viscosity and thermal conductivity of a gas mixture, such as air. These resultant transport properties may then be used as inputs to vehicle flow field calculations.

The evaluation of the collision integrals of Equation (1) requires knowledge of the collision cross sections $Q_n(E)$ for a broad range of values of the parameter, E. These cross sections can be calculated from classical scattering theory or determined from quantum mechanical scattering phase shifts. At high energies, the classical scattering approximation is valid and the cross sections may be evaluated from

$$Q_n(E) = 2\pi \int_0^\infty b(1 - \cos^n \chi) db, \text{ where} \quad (2)$$

$$\chi = \pi - 2b \int_{r_t}^\infty \frac{dr}{r^2 F(r)}$$

In these equations, b is the impact parameter and χ is the angle of deflection (See Figure 1); r_t is the classical "turning point", the largest root of

$$F(r) \equiv \left[1 - \frac{V(r)}{E} - \frac{b^2}{r^2} \right]^{1/2} = 0,$$

and V(r) is the interaction energy of the collision partners.

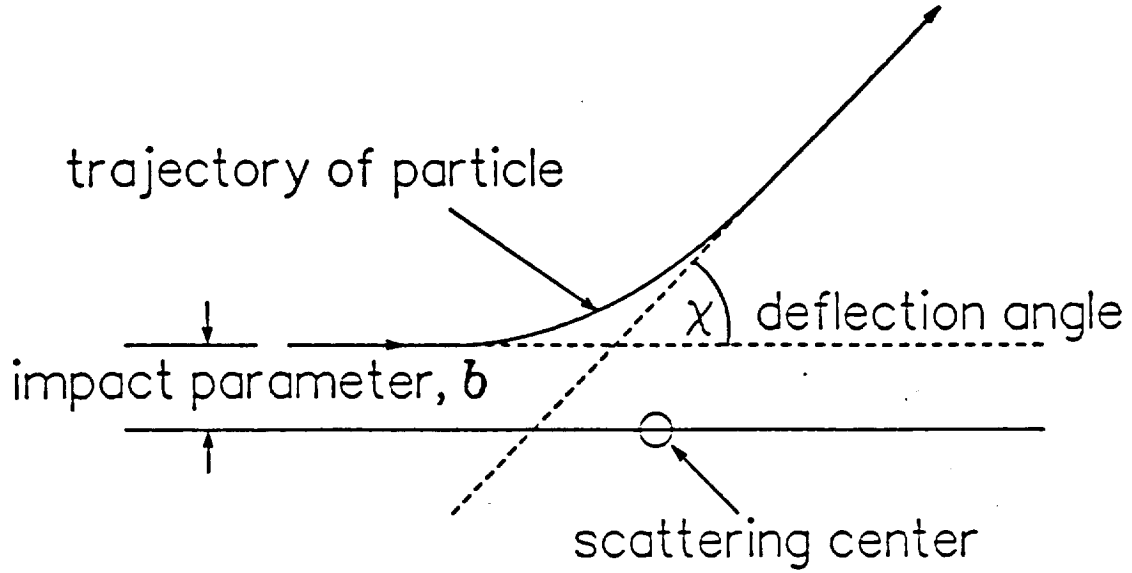


Figure 1. Scattering Geometry

The corresponding quantum theory expressions for the transport cross sections, Q_n , for ion-atom collisions are shown below [7]:

$$Q_n = \frac{1}{2} [Q_n^+ + Q_n^-] + \frac{(-1)^{2s + \Delta}}{2(2s + 1)} [Q_n^+ - Q_n^-], \quad (4)$$

where $\Delta = 0, 1, 2, \dots$ for the $\Sigma, \Pi, \Delta, \dots$ etc., states,

and s is the nuclear spin, e.g., $s = \begin{cases} 1 & \text{for nitrogen,} \\ 0 & \text{for oxygen.} \end{cases}$

For odd values of n ,

$$Q_n^+ = \frac{4\pi}{k^2} \sum_{\nu_{\text{odd}} > 0}^n [Q_{\text{odd}}(g, u; \nu) + Q_{\text{even}}(u, g; \nu)] \quad (5a)$$

$$Q_n^- = \frac{4\pi}{k^2} \sum_{\nu_{\text{odd}} > 0}^n [Q_{\text{even}}(g, u; \nu) + Q_{\text{odd}}(u, g; \nu)] \quad (5b)$$

and, for even values of n ,

$$Q_n^+ = \frac{4\pi}{k^2} \sum_{\nu_{\text{even}} > 0}^n \left[Q_{\text{even}}(g, g; \nu) + Q_{\text{odd}}(u, u; \nu) \right] \quad (6a)$$

$$Q_n^- = \frac{4\pi}{k^2} \sum_{\nu_{\text{even}} > 0}^n \left[Q_{\text{odd}}(g, g; \nu) + Q_{\text{even}}(u, u; \nu) \right] \quad (6b)$$

where,

$$Q_{\text{even}}(g, u; \nu) = \sum_{l_{\text{even}}}^{\infty} a_{n\nu}^l \sin^2(\eta_{l+\nu}^g - \eta_l^u)$$

$$Q_{\text{odd}}(g, u; \nu) = \sum_{l_{\text{odd}}}^{\infty} a_{n\nu}^l \sin^2(\eta_{l+\nu}^g - \eta_l^u)$$

In these expressions, g and u refer to the *gerade* and *ungerade* states respectively, and l is the angular momentum quantum number.

The coefficients $a_{n\nu}^l$ are determined by recursion from

$$(2l + 1) x^n P_l(x) = \sum_{\nu=-n}^n a_{n\nu}^l P_{l+\nu}(x)$$

where $P_l(x)$ are the Legendre Polynomials [8]. The charge exchange cross section is given by

$$Q_{\text{ex}} = \frac{4\pi}{k^2} \sum_{l=0}^{\infty} \frac{(2l + 1)}{4} \sin^2(\eta_l^g - \eta_l^u) \quad (7)$$

The transport cross sections for neutral atom-atom collisions were calculated from

$$Q_n = \frac{4\pi}{k^2} \sum_{\nu > 0}^n \sum_{l=0}^{\infty} a_{n\nu}^l \sin^2(\eta_{l+\nu} - \eta_l), \quad (8)$$

where the allowed values of ν are $\left\{ \begin{matrix} \text{even} \\ \text{odd} \end{matrix} \right\}$ according to the even or odd parity of n .

At high energies, the scattering phase shifts η_l are approximated by the JWKB formula,

$$\frac{\eta_{\text{jwkb}}}{k} = \int_{r_3}^{\infty} \left\{ G(r) \right\}^{\frac{1}{2}} dr - \int_{\beta}^{\infty} \left\{ 1 - \frac{\beta^2}{r^2} \right\}^{\frac{1}{2}} dr \quad (9)$$

The lower limit r_3 of the first integral is the largest root of

$$G(R) \equiv 1 - \frac{V(R)}{E} - \frac{\beta^2}{R^2} = 0.$$

In Equation 9, $\beta = (l + 1/2)/k$ can be identified with the classical impact parameter b .

At low energies, we apply a semiclassical method that accounts for tunnelling through the barrier of the effective potential energy (see Fig. 2). The uniform phase shift approximation developed by Stallcop [4] also accounts for resonance scattering associated with metastable energy levels of the inner potential well and virtual energy levels above the barrier minimum.

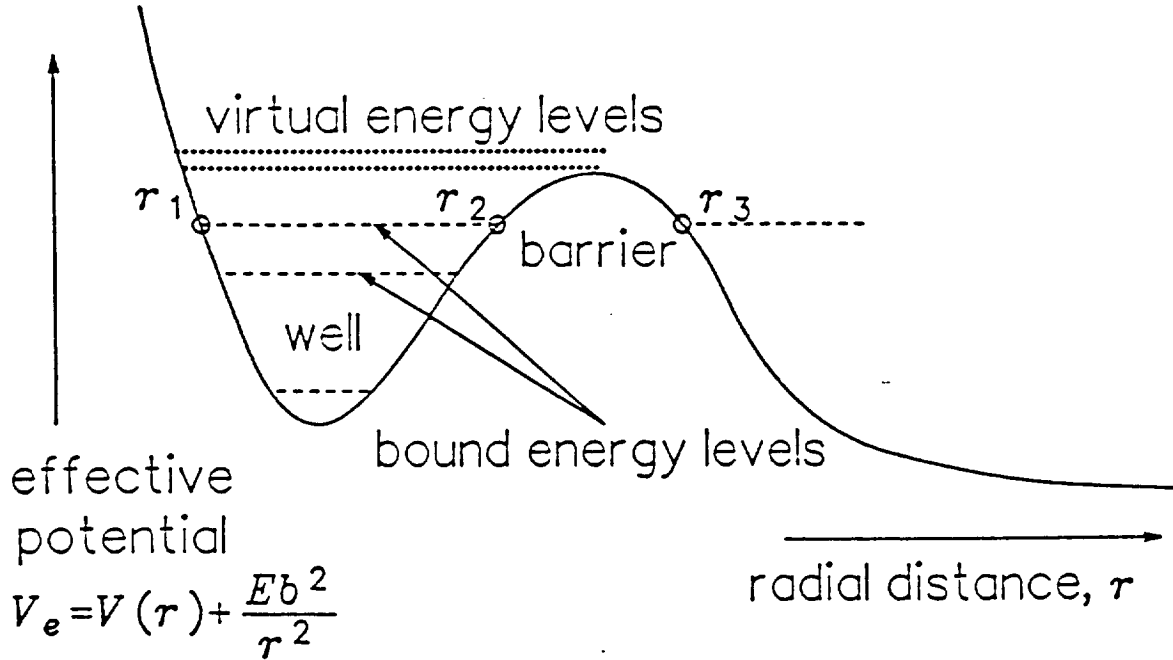


Figure 2. Effective Potential Energy, V_e

For energy levels below the barrier,

$$\eta = \eta_{\text{jwkb}} + \rho + \arctan \left\{ \frac{\sqrt{1 + e^{-2(I + \tau)}} - 1}{\sqrt{1 + e^{-2(I + \tau)}} + 1} \tan(\phi + \rho) \right\}, \text{ where}$$

$$\rho = 0.5 \arg \Gamma \left\{ \frac{1}{2} + \frac{iI}{\pi} \right\} - \frac{I}{2\pi} \ln \left| \frac{I}{e\pi} \right|,$$

$$\tau = 0.5 \ln \left\{ \Gamma \left(\frac{1}{2} + \frac{\phi}{\pi} \right) / \sqrt{2\pi} \right\} - \frac{\phi}{2\pi} \ln \left| \frac{\phi}{e\pi} \right|,$$

$$\phi = k \int_{r_1}^{r_2} [G(r)]^{1/2} dr,$$

$$I = k \int_{r_2}^{r_3} |G(r)|^{1/2} dr,$$

and r_1, r_2, r_3 are the ordered roots of $G(r)=0$.

For energy levels above the barrier, there is only one root, r_1 , and η takes the form

$$\eta = \eta_{\text{jwkb}} + 2\rho - \arctan \left\{ \frac{\sin 2(\phi + \rho)}{\sqrt{1 + e^{-2I}} + \cos 2(\phi + \rho)} \right\}, \text{ where now,}$$

$$\phi = k \int_{r_1}^{r_m} [G(r)]^{1/2} dr,$$

$$\rho = 0.5 \arg \Gamma \left\{ \frac{1}{2} + \frac{iI}{\pi} \right\} - \frac{I}{2\pi} \ln \left| \frac{I}{e\pi} \right|, \text{ and}$$

$$I = \frac{-\pi k}{\sqrt{2}} \left\{ \frac{G}{\sqrt{|G'|}} \right\}_{r=r_m}.$$

The quantity $r=r_m$ specifies the position of the barrier maximum. The expression for I is based on a local parabolic expansion near the barrier maximum.

III. SOURCES OF INTERACTION ENERGY DATA

The interaction energies (which correspond to the potential energy curves of the various states of the molecules formed from the colliding atom-atom or ion-atom pairs) are needed as input to determine the transport cross sections. We have combined experimental data with the results of *ab initio* molecular structure calculations to obtain the best representation of the true interaction energies.

For example, where available we have used experimental data such as the measured dissociation energy [12] and RKR turning points to represent the potential in the region of the well minimum. *Ab initio* molecular structure potential calculations were used to extend the experimental data to the adjoining regions by adjusting the *ab initio* results to agree with the experimental data. Since electron exchange interactions dominate in this region (i.e., the potential energy behaves roughly like an exponential function $V_0 e^{-\alpha R}$), the adjustments were made in such a way as to preserve the value of the shielding parameter, α . For small R , where the potential curves are steep, we have shifted the *ab initio* potentials by ΔR , the difference between the calculated and measured equilibrium separation distance R_e . Since the measured and calculated values of the potential curves are in good agreement (e.g., Ref. [1]), the transport cross sections are not very sensitive to the manner of adjusting the *ab initio* results to be compatible with the measured data.

The *ab initio* interaction curves have been extended by a proper form of the long range potential interaction. For the neutral atom-atom interactions, such as N-N and O-O, we use the potential form $-C_6 R^{-6}$. The ion-atom N^+-N interaction exhibits the charge-induced dipole force $-\frac{1}{2}\alpha R^{-4}$, whereas the O^+-O interaction behaves like a charge-quadrupole potential $\frac{1}{2}Q_M R^{-3}$. The quadrupole moment Q_M is negative for Σ state interactions, but is *positive* for Π states [13]. The values of the parameters C_6 , α and Q_M have been determined either from the *ab initio* results at large R or taken directly from other approximations to the Schroedinger equation such as perturbation expansions [14].

We now describe in detail the source of all the potential curves; we begin with N-N. The potential wells of the bound states $X^1\Sigma_g^+$ and $A^3\Sigma_u^+$ of N_2 were obtained from RKR data [15,16]. Additional potential information for these states and also for the $^5\Sigma_g^+$ state was derived from the configuration interaction studies of Ermler, McLean and Mulliken [17]. The repulsive region of the ground state $X^1\Sigma_g^+$ was extended to small R with the help of the generalized valence bond calculations of Dunning, Cartwright, Hunt, Hay and Bobrowicz [18] and Guberman [19]. The $^5\Sigma_g^+$ potential was extended to large R with the MC-SCF results of Krauss and Neumann [20]. The $^7\Sigma_u^+$ state potential has been computed accurately by Partridge, Langhoff and Bauschlicher [21]; these results have been extended to smaller R by adjusting the SCF potential determined by Ferrante and Stwalley [22]. The long range calculations of [21] strongly support the value of the dispersion coefficient deduced by Zeiss and Meath [14]; consequently, we have used their values for all the long range N-N interactions.

The sources of the O-O interactions will be described next. Saxon and Liu [23] have performed configuration interaction calculations for the 62 electronic states of O_2 that dissociate into O atoms in their lowest 3P , 1D , and 1S states. We find that the values of C_6 deduced from their large R results are consistent with those of Neumann and Krauss [24]. The Saxon and Liu results have been used directly for collisions involving excited state atoms. For ground state O-O interactions we have made the following modifications to the Saxon and Liu curves. The potential wells of the $X^3\Sigma_g^-$, $a^1\Delta_g$, $b^1\Sigma_g^+$, and the $A^3\Sigma_u^+$ states of O_2 have been determined from RKR data [25]. Spectroscopic data for the other two bound states were used to determine the parameters of an HH potential function [26,27]. The *ab initio* results were then adjusted to the curve obtained from this potential fit in the region of the well minimum in the same manner described above for the RKR curves.

In addition, we have included corrections for some Rydberg states and shifted energies at small R to give better agreement with electron scattering measurements. The Rydberg character of the $^3\Pi_u$ state at small R has been taken into account using the potentials calculated by Buenker and Peyerimhoff [28] and Guberman and Dalgarno [29]. Similarly, Rydberg corrections to the $^3\Pi_g$ and $^1\Pi_g$ states have been taken from Saxon and Liu [30,31]. Furthermore, the potential curves of the $^3\Pi_u$, and $^3\Pi_g$ states have been shifted at small R to be consistent with the potentials deduced from electron scattering measurements [32,33,34].

Our calculations of the N^+-N interaction curves using a CASSCF method has been described previously [1,2,3]. Primarily the results from the large basis set [2] have been used for the transport calculations of this work. We have, however, augmented the data from this large basis set with additional data points deduced from the small basis set calculations. This was accomplished by shifting the energies of the small basis set by an amount determined by a parabolic interpolation of the energy differences between the two basis sets. These additional data points are especially useful in the regions of the potential wells and avoided crossings.

The wells of the bound states $X^2\Sigma_g^+$, $A^2\Pi_u$, and $^2\Pi_g$ were obtained from RKR data [25]. The potential curve extracted from spectroscopic data by Hajj [35] was used for the $B^2\Sigma_u^+$ state well region.

Our calculated potentials for the O^+-O interactions are shown in paper [1]. We have modified these curves with RKR data for the bound states $X^2\Pi_g$, $A^2\Pi_u$, and $a^4\Pi_u$. The long range quadrupole parameter Q_M was obtained from the calculated energies at large R after first subtracting the single electron exchange contribution [2].

A summary listing of all the states for which we calculated transport cross sections is shown in Table 1. The weights shown following the state designations represent the degree of degeneracy (multiplicity) of that state and must be considered in the determination of *mean* collision cross sections. The potentials employed are contained in a report [36] which is available upon request.

Table 1. LISTING OF STATES ANALYZED

O-O STATES (WEIGHTS)					
GROUND	EXCITED				
$O(^3P)-O(^3P)$	$O(^3P)-O(^1D)$	$O(^1D)-O(^1D)$	$O(^3P)-O(^1S)$	$O(^1D)-O(^1S)$	$O(^1S)-O(^1S)$
$b^1\Sigma_g^+ (1)$	$B^3\Sigma_u^- (3)$	$2^1\Sigma_u^- (1)$	$3^3\Sigma_u^- (3)$	$1^1\Sigma_u^+ (1)$	$7^1\Sigma_g^- (1)$
$c^1\Sigma_u^- (1)$	$^3\Sigma_g^+ (3)$	$3^1\Sigma_u^- (1)$	$4^3\Sigma_g^- (3)$	$6^1\Sigma_g^+ (1)$	
$2^1\Sigma_g^+ (1)$	$2^3\Sigma_u^- (3)$	$3^1\Sigma_g^+ (1)$	$5^3\Pi_g (6)$	$4^1\Pi_g (2)$	
$X^3\Sigma_g^- (3)$	$2^3\Sigma_g^- (3)$	$4^1\Sigma_g^+ (1)$	$5^3\Pi_u (6)$	$4^1\Pi_u (2)$	
$A^3\Sigma_u^+ (3)$	$3^3\Sigma_u^+ (3)$	$5^1\Sigma_g^+ (1)$		$2^1\Delta_u (2)$	
$2^3\Sigma_u^+ (3)$	$3^3\Sigma_g^- (3)$	$2^1\Pi_g (2)$		$4^1\Delta_g (2)$	
$^5\Sigma_u^- (5)$	$2^3\Pi_g (6)$	$2^1\Pi_u (2)$			
$1^5\Sigma_g^+ (5)$	$2^3\Pi_u (6)$	$3^1\Pi_g (2)$			
$2^5\Sigma_g^+ (5)$	$3^3\Pi_g (6)$	$3^1\Pi_u (2)$			
$1^1\Pi_g (2)$	$3^3\Pi_u (6)$	$1^1\Delta_g (2)$			
$1^1\Pi_u (2)$	$4^3\Pi_g (6)$	$2^1\Delta_g (2)$			
$1^3\Pi_g (6)$	$4^3\Pi_u (6)$	$3^1\Delta_u (2)$			
$1^3\Pi_u (6)$	$1^3\Delta_g (6)$	$^1\Phi_g (2)$			
$^5\Pi_g (10)$	$2^3\Delta_g (6)$	$^1\Phi_u (2)$			
$^5\Pi_u (10)$	$2^3\Delta_u (6)$	$^1\Gamma_g (2)$			
$a^1\Delta_g (2)$	$3^3\Delta_g (6)$				
$C^3\Delta_u (6)$	$^3\Phi_g (6)$				
$^5\Delta_g (10)$	$^3\Phi_u (6)$				
$N(^4S^o)-N(^4S^o)$		$N^+(^3P)-N(^4S^o)$		$O^+(^4S^o)-O(^3P)$	
$X^1\Sigma_g^+ (1)$		$2^2\Sigma_g^+, 2^2\Sigma_u^+ (2)$		$2^2\Sigma_g^+, 2^2\Sigma_u^+ (2)$	
$A^3\Sigma_u^+ (3)$		$4^4\Sigma_g^+, 4^4\Sigma_u^+ (4)$		$4^4\Sigma_g^+, 4^4\Sigma_u^+ (4)$	
$^5\Sigma_g^+ (5)$		$6^6\Sigma_g^+, 6^6\Sigma_u^+ (6)$		$6^6\Sigma_g^+, 6^6\Sigma_u^+ (6)$	
$7^7\Sigma_u^+ (7)$		$2^2\Pi_g, 2^2\Pi_u (4)$		$2^2\Pi_g, 2^2\Pi_u (4)$	
		$4^4\Pi_g, 4^4\Pi_u (8)$		$4^4\Pi_g, 4^4\Pi_u (8)$	
		$6^6\Pi_g, 6^6\Pi_u (12)$		$6^6\Pi_g, 6^6\Pi_u (12)$	

Figure 3 is a plot of the potential curves of the 18 states of O_2 that dissociate into oxygen atoms in the 3P state. The discrete data points are shown along with the resulting spline fit. The corresponding curves for $N-N$, O^+-O , and N^+-N for dissociation into ground state ion-atom pairs are shown in Figures 4, 5, and 6, respectively. Figure 7 shows the spline fits to the discrete data for $O-O$ in their lowest states as well as the five excited states. (The discrete data points used to generate these plots have been omitted for clarity.)

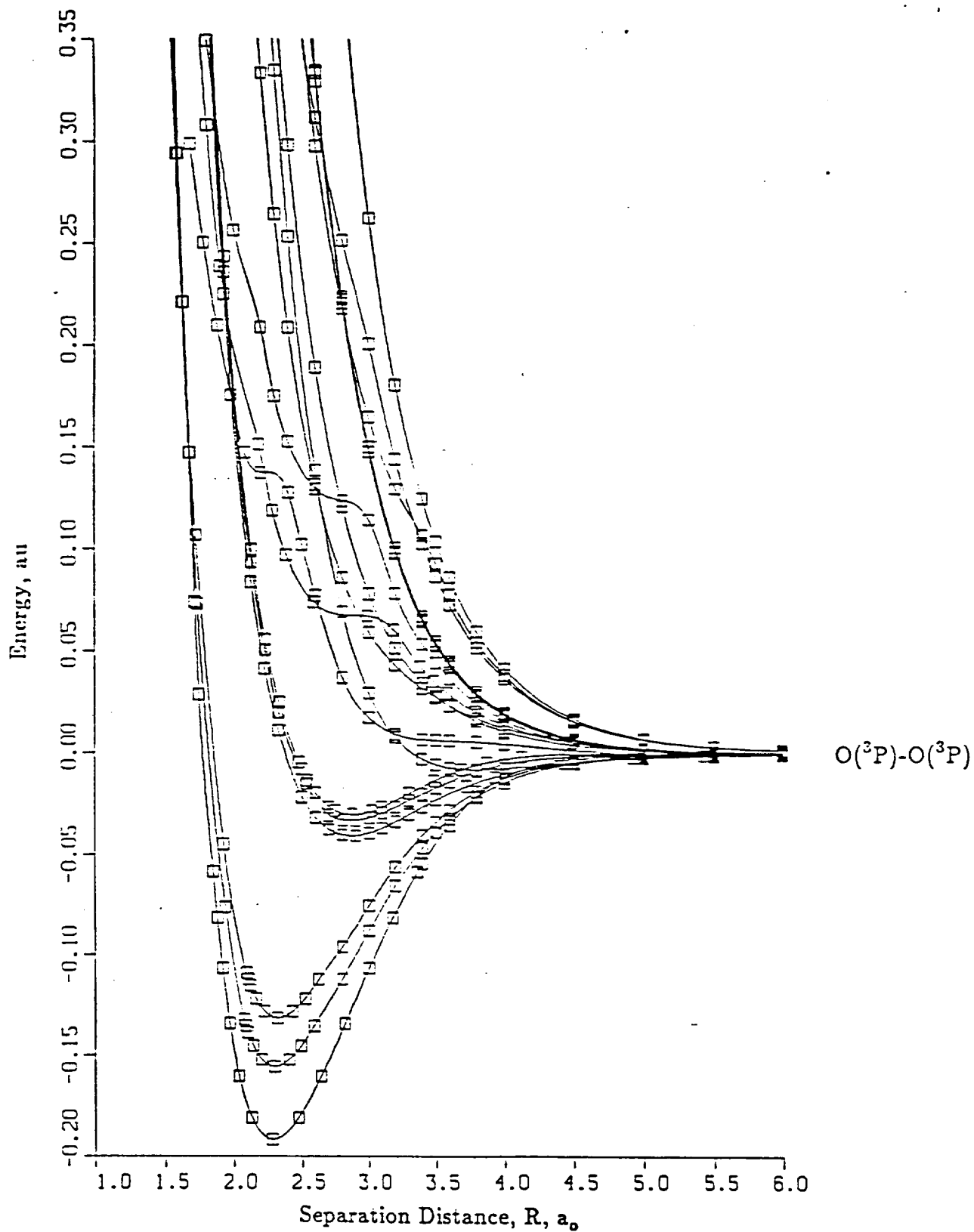


Figure 3. $O(^3P)-O(^3P)$ Interaction Energies

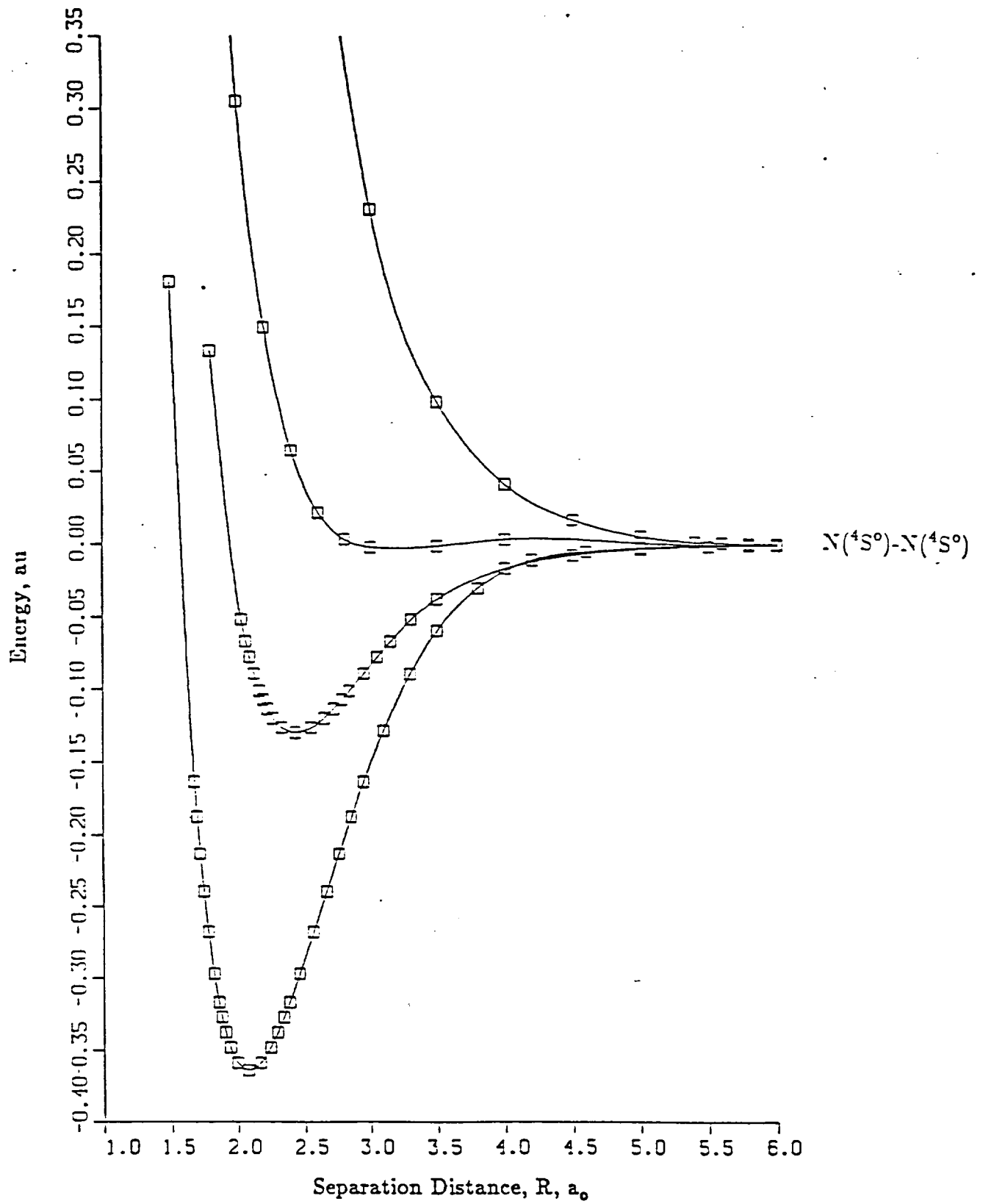


Figure 4. N($4S^\circ$)-N($4S^\circ$) Interaction Energies

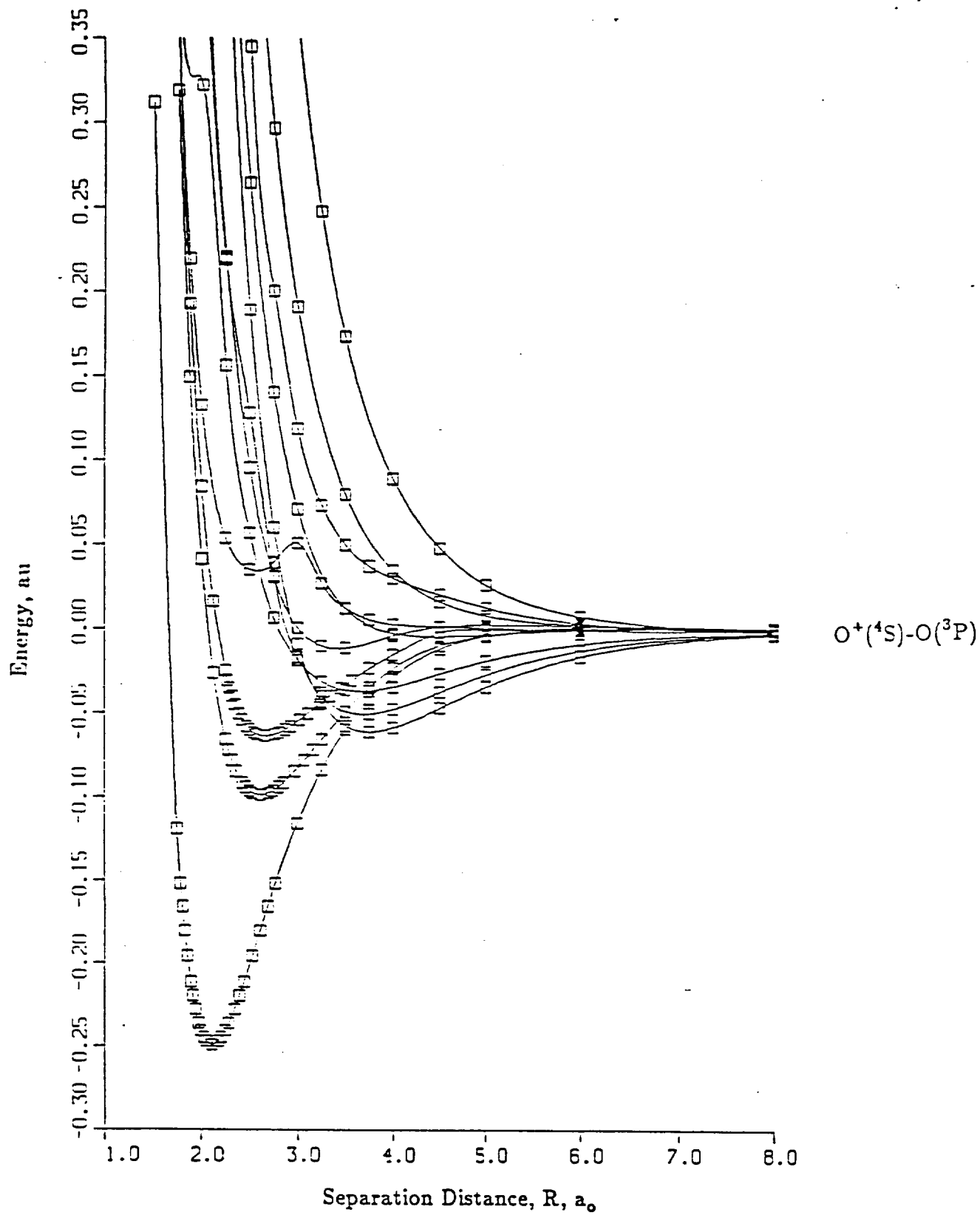


Figure 5. $O^+(^4S)-O(^3P)$ Interaction Energies

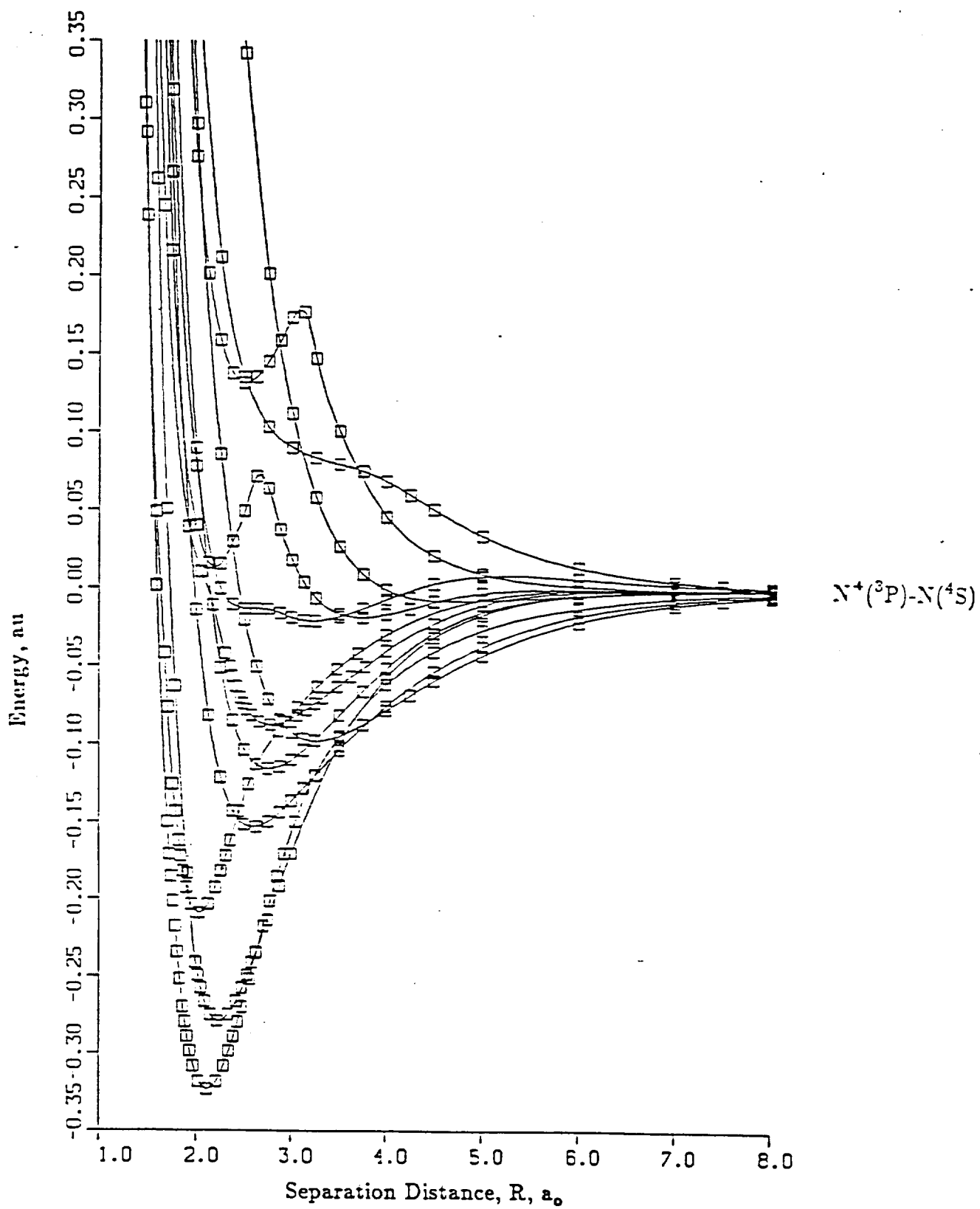


Figure 6. $N^+(^3P)-N(^4S)$ Interaction Energies

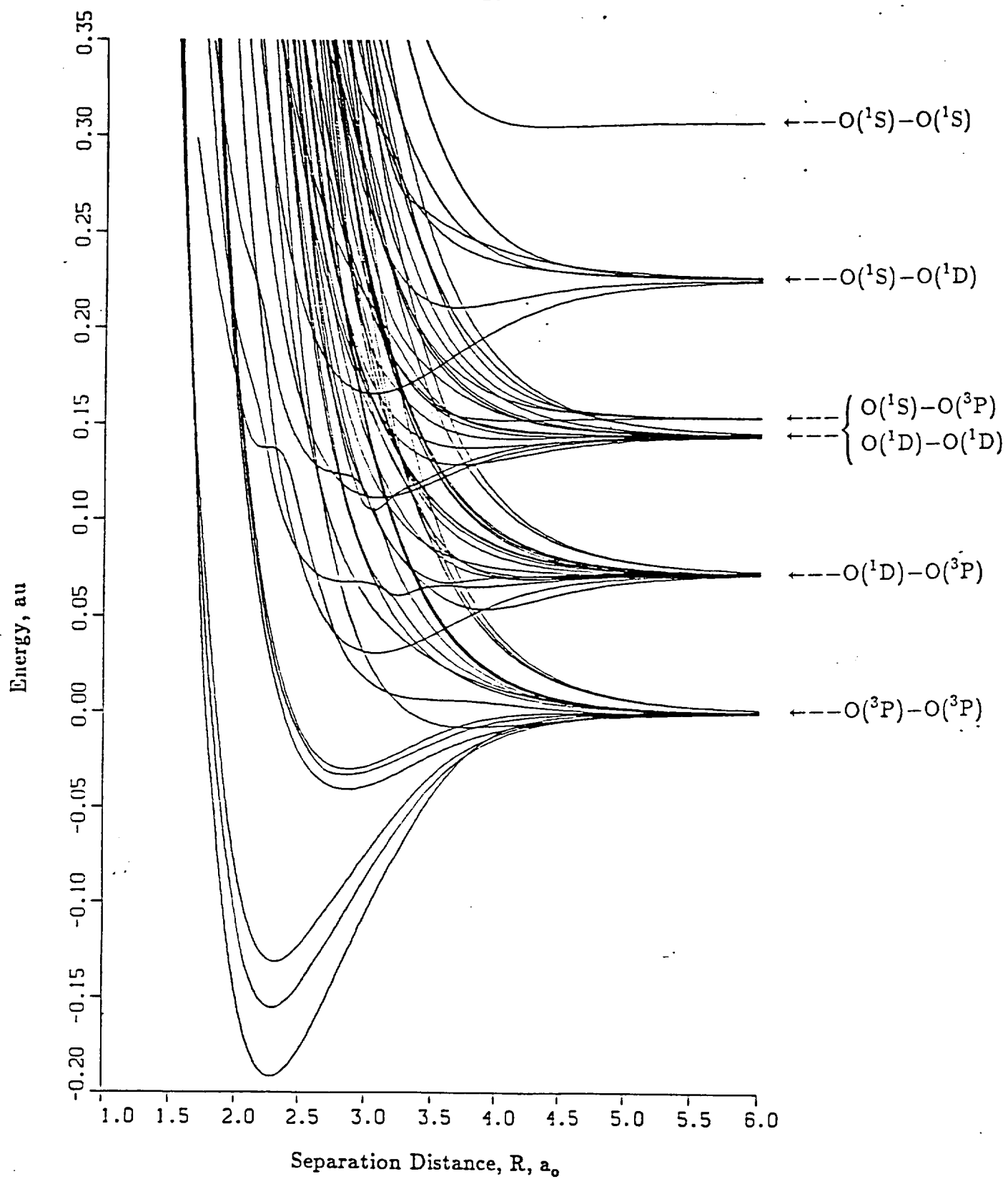


Figure 7. Ground State and Excited State O-O Interaction Energies

IV. THE SKATR COMPUTER PROGRAM

The SKATR program fits a spline curve to the discrete potential data and accepts any long range interactions of the general form

$$V(R) = A_1 R^n e^{-A_2 R} + \frac{A_3}{R^3} + \frac{A_4}{R^4} + \frac{A_5}{R^5} + \frac{A_6}{R^6}.$$

For small values of R, the program determines the parameters of an exponential function to agree with the spline fit and the first derivative of the spline at the beginning of the discrete potential data. A typical input data set is shown in Table 2.

Table 2. Potential Data for O-O State X $^3\Sigma_g^-$	
R (a ₀)	V(R) (a.u.)
1.54700	0.36800
1.58700	0.29400
1.62700	0.22100
1.67700	0.14700
1.71700	0.07400
1.74700	0.02825
1.84740	-0.05864
1.87710	-0.08165
1.91560	-0.10686
1.96850	-0.13417
2.03840	-0.16021
2.13020	-0.18084
2.28195	-0.19151
2.47160	-0.18084
2.64110	-0.16021
2.81890	-0.13417
3.00070	-0.10686
3.17940	-0.08165
3.36410	-0.05864
3.40000	-0.05456
3.60000	-0.03560
3.80000	-0.02141
4.00000	-0.01222
4.50000	-0.00333
5.00000	-0.00145
5.50000	-0.00078
6.00000	-0.00047
6.50000	-0.00030
7.00000	-0.00019
FOR R<1.547, V(R) = 893.31 e ^(-5.0385R)	
FOR R>7.000, V(R) = -401.9 e ^(-2.6002R) - $\frac{22.0}{R^6}$	

The SKATR program uses the interaction potential to determine the *effective* potential,

$$V_e(R) = V(R) + \frac{(l+1/2)^2 E}{k^2 R^2},$$

for increasing values of the angular momentum quantum number l . The maxima and minima of the effective potential are located and the turning points are determined for a large set of energies. This permits the phase shifts to be evaluated using the appropriate semiclassical formulas. The process is continued until the running sum for determining the collision cross sections satisfies a convergence criterion.

Numerous tests were conducted to validate the code including those described below. **Check on η_{jwkb} ;** Cohen [9] reports the results of accurate calculations of η_{jwkb}/kr_e for a variety of potential functions and various energies. The values reported by Cohen have a stated accuracy of five decimal places. For the Morse potential,

$$V(r) = D_e \left[e^{-2\alpha(r-r_e)} - 2e^{-\alpha(r-r_e)} \right]$$

with $\alpha r_e = 3$, $D_e = 0.324$, and $r_e = 2.12$, six cases were compared corresponding to $E/D_e = 0.01$ and 0.8 with $\beta/r_e = 0.25, 1.00, 1.50$. It was found that our results agreed *precisely* with those of Cohen to five decimal places.

Check on Q_n ; Equation (2) is applicable at high energies and the SKATR program can be applied at all energies (although it is quite inefficient to do so when the quantum effects are negligible). For the Morse potential (given above) and $E > 0.15$ a.u., the energy is above the barrier of the *effective* potential (see Figure 2). Table 3 shows the results of the SKATR program compared with the classical results for the collision cross sections. (The mass of each collision partner was taken to be equal to that of nitrogen.) The values of the cross sections listed are obtained from Equation (2) using a code developed by Galant [10] and δ is the difference between the classical and the quantum mechanical results. As the energy increases, the corrections become less significant as expected.

Table 3. Comparison With Classical Calculation						
E (a.u.)	Q_1	δ_1	Q_2	δ_2	Q_3	δ_3
0.15	59.67	7.2 (-2)	40.07	-3.7 (-2)	65.74	8.5 (-3)
0.25	39.56	3.8 (-4)	38.12	-5.7 (-3)	47.17	-3.2 (-3)
0.50	17.41	1.8 (-4)	21.72	1.5 (-4)	28.82	-1.0 (-3)
0.80	11.14	-8.0 (-6)	12.97	1.2 (-4)	17.97	-1.6 (-4)

Successful tests of Q_n were also done using a Lennard-Jones potential of the form, $V(r) = 4 D_e (r^{-12} - r^{-6})$ and comparing the results with O'Hara and Smith [11].

V. RESULTS

Principal results along with selected illustrative examples of intermediate results are presented in this section. A complete tabulation is contained in a report [36]. Using the input data set shown in Table 1, we evaluated the semiclassical equations to determine the phase shifts and subsequently the collision cross sections Q_1 , Q_2 , and Q_3 . Since the Q_n are needed as functions of energy for the subsequent evaluation of the collision integrals (Eqn. (1)), this evaluation was done for a set of 40 E values from 10^{-4} a.u. to 1.90 a.u. For each of the higher energy cases, the program typically required about 1500-2000 values of the angular momentum quantum number to assure convergence of the infinite summation of Equation (8) to five significant figures. For very low energies, about 500 values of l were typically required for convergence. The running time on the Cray XMP-4/8 for the entire set of 40 energy values (corresponding to $\approx 40,000$ phase shifts η_l) was about two minutes for each state. A small subset of the results is shown in Table 4; the cross sections Q_n are expressed in units of a_0^2 , where a_0 is the Bohr radius.

E (a.u.)	Q_1	Q_2	Q_3
1.50 (-0)	6.521 (+0)	6.470 (+0)	8.860 (+0)
5.00 (-1)	1.291 (+1)	1.477 (+1)	2.012 (+1)
1.00 (-1)	4.319 (+1)	2.980 (+1)	4.748 (+1)
5.00 (-2)	4.680 (+1)	3.433 (+1)	5.226 (+1)
1.00 (-2)	5.642 (+1)	4.721 (+1)	6.629 (+1)
5.00 (-3)	7.856 (+1)	5.854 (+1)	9.104 (+1)
1.00 (-3)	1.349 (+2)	1.026 (+2)	1.591 (+2)

In order to obtain the mean collision integrals for $O(^3P) + O(^3P)$ collisions, each of the 18 states listed in the first column of Table 1 was processed as described above and combined according to their degree of degeneracy to yield weighted mean collision cross sections Q_n . A sample of the results is shown in Table 5 and in graphical form in Figure 8. It was also of interest to investigate the contribution of each of the states to the mean collision cross sections. Table 6 shows the contribution of each $O(^3P)-O(^3P)$ state to the mean cross section Q_1 . Similar tables were prepared for the mean values of Q_2 , and Q_3 , and the process was repeated for all the excited states of Table 1. The results emphasize that the high spin, largely repulsive states are extremely important contributors to the collision cross-sections and hence to the transport properties.

For like ion-atom collisions such as N^+-N , the phase shifts for each *gerade* and *ungerade* pair of states are combined to determine the cross sections according to Eqs.(4)-(7). Table 7 illustrates a sample of the resulting cross sections for an N^+-N interaction. Note that Q_1 and Q_3 approach a value $2Q_{ex}$ at high energies as expected; at low energies where the induced dipole polarization force becomes important, this simple relationship is no longer valid.

TABLE 5. MEAN $O(^3P)-O(^3P)$ CROSS SECTIONS

E (a.u.)	MEAN Q_1	MEAN Q_2	MEAN Q_3
1.50	8.3843	9.8475	1.2629 (+1)
5.00 (-1)	1.6288 (+1)	1.5755 (+1)	2.1214 (+1)
1.00 (-1)	3.1451 (+1)	2.7872 (+1)	3.8382 (+1)
5.00 (-2)	3.9492 (+1)	3.3994 (+1)	4.6898 (+1)
1.00 (-2)	6.1801 (+1)	5.2321 (+1)	7.2494 (+1)
5.00 (-3)	7.5134 (+1)	6.1451 (+1)	8.7187 (+1)
1.00 (-3)	1.1891 (+2)	9.9196 (+1)	1.4022 (+2)

TABLE 6. CONTRIBUTION (%) OF EACH $O(^3P)-O(^3P)$ STATE TO WEIGHTED MEAN Q_1

STATE	WT.	ENERGY (a.u.)						
		1.5	0.5	0.1	0.05	0.01	0.005	0.001
$b^1\Sigma_g^+$	1	1	1	2	2	1	1	1
$c^1\Sigma_u^+$	1	1	1	1	1	2	1	1
$2^1\Sigma_g^+$	1	1	2	2	2	2	1	1
$X^3\Sigma_g^-$	3	3	3	5	4	3	4	4
$A^3\Sigma_u^+$	3	3	3	2	3	3	3	3
$2^3\Sigma_u^+$	3	3	5	5	5	5	4	4
$1^5\Sigma_u^-$	5	7	7	6	6	6	5	5
$1^5\Sigma_g^+$	5	9	8	8	7	6	6	5
$2^5\Sigma_g^+$	5	10	10	8	8	8	7	6
$1^1\Pi_g$	2	1	2	3	3	2	2	3
$1^1\Pi_u$	2	2	2	2	2	2	2	2
$1^3\Pi_g$	6	5	4	6	7	7	7	6
$1^3\Pi_u$	6	3	4	5	5	5	6	10
$1^5\Pi_g$	10	14	13	10	10	15	16	19
$1^5\Pi_u$	10	15	16	14	13	12	12	10
$a^1\Delta_g$	2	2	2	4	3	3	3	2
$C^3\Delta_u$	6	6	5	5	7	6	6	7
$5^5\Delta_g$	10	15	16	14	13	12	12	10

TABLE 7. COLLISION CROSS SECTIONS FOR $N^+(^3P)-N(^4S^o)$ PAIR [$^4\Sigma_g^+$, $^4\Sigma_u^+$]

E (a.u.)	Q_1	Q_2	Q_3	Q_{ex}
0.5	3.2129 (+2)	1.1953 (+1)	3.2096 (+2)	1.5992 (+2)
0.15	3.7586 (+2)	3.8853 (+1)	3.7606 (+2)	1.8772 (+2)
0.05	4.2311 (+2)	6.3146 (+1)	4.2401 (+2)	2.0815 (+2)
0.005	5.5623 (+2)	1.7158 (+2)	5.5643 (+2)	2.6724 (+2)
0.0005	8.4220 (+2)	4.4297 (+2)	8.7678 (+2)	3.5775 (+2)

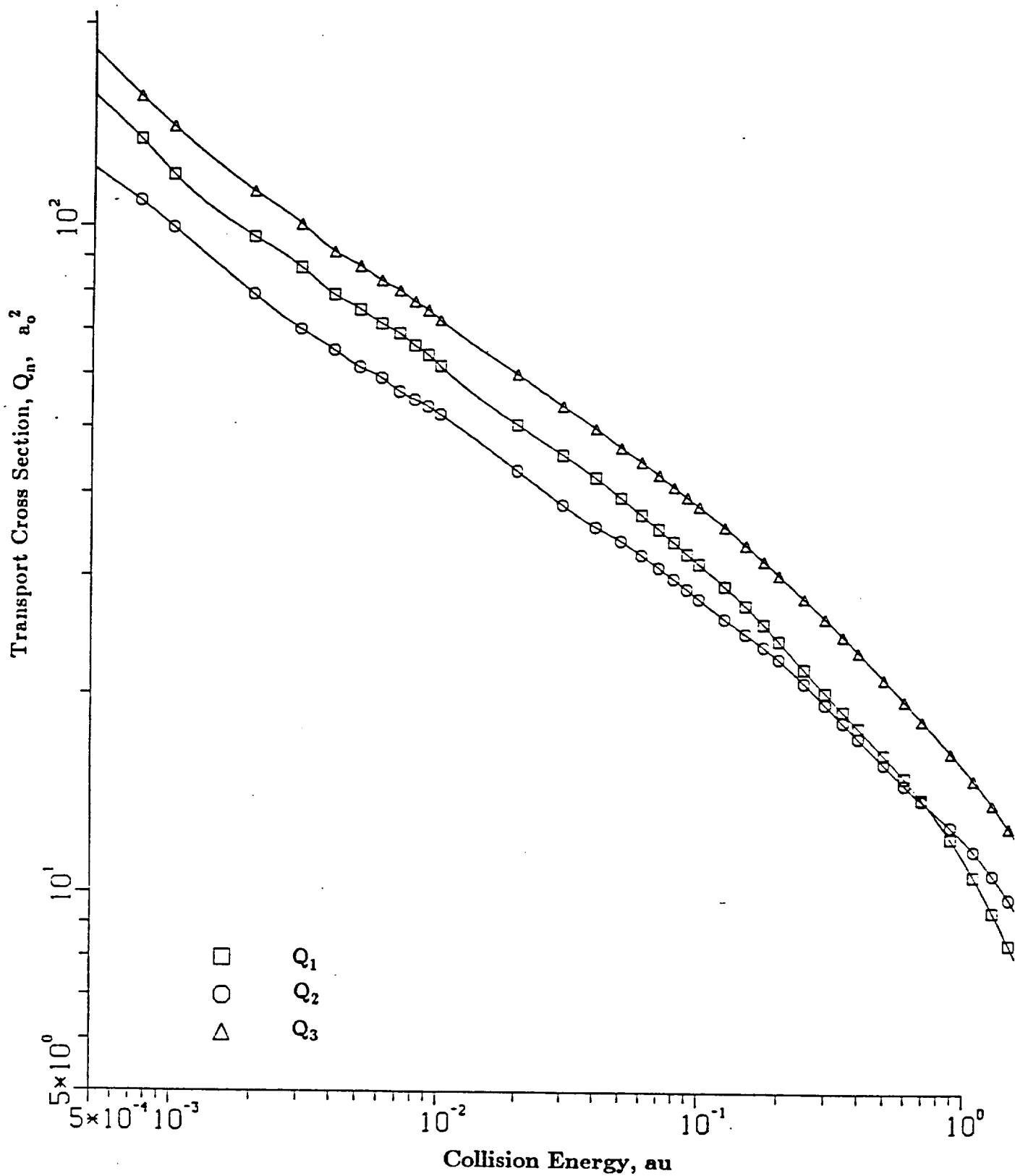


Figure 8. Mean Transport Cross Sections, $O(^3P)-O(^3P)$

The resonance charge exchange cross sections have been determined with the present code and the results are displayed in Figure 9 along with the asymptotic approximation of Stallcop and Partridge [2] and available measured data from beam experiments [37,38]. Both the present "exact" results and prior approximate theoretical values agree with the measured data to within the experimental uncertainty. Hence, the present calculations give further support to the reliability of our calculated values of the long-range ion-atom interaction. Furthermore, a comparison of theoretical and experimental values provides a means to assess the contribution of excited state interactions. This contribution is expected to become appreciable at high energies; however, the results displayed in Figure 9 indicate it is small for the range of energies of the present work.

Some principal results of the present study are summarized in Tables 8-11, which show the nine collision integrals (in units of square Angstroms= 10^{-16} cm²) needed for the determination of the transport properties of a pure gas to second order or a gas mixture to first order. These tables represent the ground state O-O, N-N, O⁺-O, and N⁺-N collision integrals, respectively for temperatures ranging from 250 to 100,000 K. Similar results for the excited state O-O collisions are contained in report [36].

The discrete data points were typically available only for a range of R from about 1.5 to 10.0. Outside of this range, analytic extensions to the data were used. Experiments varying the short range extrapolation showed that the final results (for both the collision cross sections as well as the collision integrals) were relatively insensitive to the specific extrapolations for small R. Similar experiments for the long range extrapolation showed quite different results. Both the functional form as well as the particular parameters selected within a functional form had a significant effect on the collision cross sections for small values of the energy (e.g., energies below ≈ 0.001 a.u.).

Furthermore, as can be seen from Figures 4-7, several potential curves exhibit potential barriers arising from avoided crossings of potential curves of other states with the same symmetry. For some states, the combination of this maximum and a well in the potential curve introduced a double barrier in the effective potential energy for low energy collisions. The resonance effects are expected to be small in this case for the scattering conditions of the present study. Consequently, a barrier treatment of the type described in Section II was not applied. The phase shifts were simply determined from the JWKB approximation. (This is equivalent to considering the region inside the outermost turning point to be inaccessible, as in a classical mechanics treatment.)

In view of the above considerations, some of the cross sections at low energies may not be accurate because of uncertainties in the long range interaction energies for some states and our approximate treatment of the double barrier cases. However, the effect of these possible low energy cross section errors on the collision integrals is sharply diminished by the presence of the factor x^{2s+3} in Equation (1).

Similarly, the uncertainty in the tabulated values of the collision integrals due to extrapolation of the potential data at small R should not be significant for two reasons. In the first place, the scattering from the repulsive walls of inner low lying

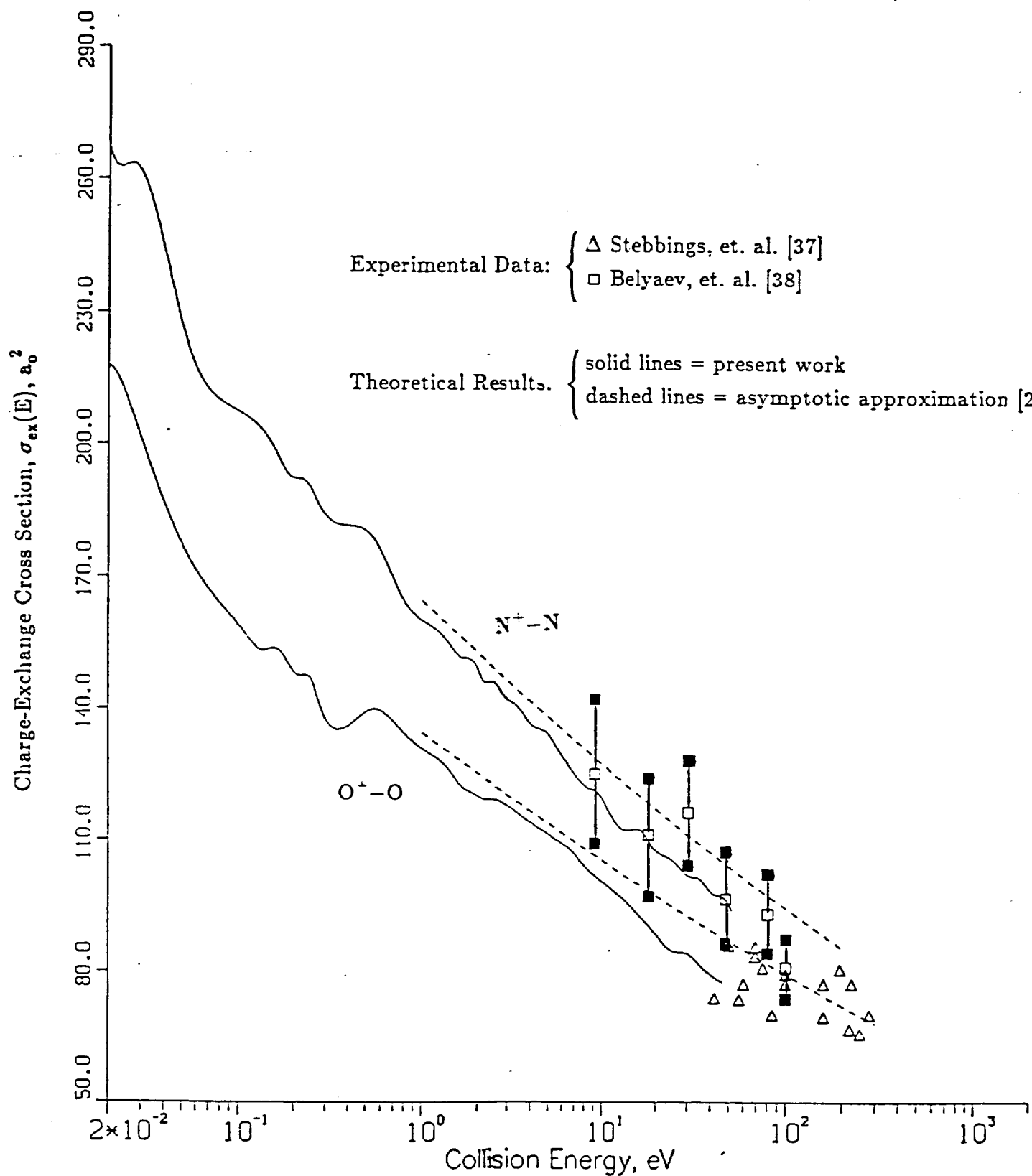


Figure 9. Resonance Charge Exchange Cross Sections

TABLE 8. MEAN COLLISION INTEGRALS, $\sigma^2 \bar{\Omega}(i,j)$, FOR $O(^3P)-O(^3P)$ COLLISIONS

TEMP K	$\sigma^2 \bar{\Omega}(1,1)$	$\sigma^2 \bar{\Omega}(1,2)$	$\sigma^2 \bar{\Omega}(1,3)$	$\sigma^2 \bar{\Omega}(1,4)$	$\sigma^2 \bar{\Omega}(1,5)$	$\sigma^2 \bar{\Omega}(2,2)$	$\sigma^2 \bar{\Omega}(2,3)$	$\sigma^2 \bar{\Omega}(2,4)$	$\sigma^2 \bar{\Omega}(3,3)$
250	8.861	7.963	7.388	6.967	7.516	9.798	9.093	8.825	8.591
300	8.390	7.565	7.032	6.635	6.858	9.310	8.666	8.301	8.173
500	7.247	6.568	6.103	5.693	5.406	8.139	7.611	7.147	7.123
750	6.466	5.858	5.424	5.024	4.714	7.345	6.857	6.379	6.380
1000	5.958	5.396	4.995	4.649	4.397	6.821	6.354	5.923	5.903
2000	4.899	4.446	4.136	3.898	3.713	5.665	5.276	4.979	4.907
3000	4.378	3.973	3.691	3.473	3.296	5.082	4.742	4.488	4.396
4000	4.039	3.657	3.386	3.176	3.005	4.707	4.392	4.152	4.055
5000	3.787	3.419	3.156	2.951	2.785	4.432	4.130	3.899	3.801
6000	3.588	3.229	2.972	2.773	2.610	4.216	3.923	3.697	3.600
7000	3.424	3.072	2.820	2.624	2.464	4.037	3.752	3.532	3.433
8000	3.284	2.939	2.690	2.497	2.340	3.886	3.607	3.391	3.290
9000	3.163	2.823	2.578	2.387	2.232	3.756	3.481	3.268	3.167
10000	3.056	2.720	2.478	2.291	2.139	3.641	3.370	3.159	3.058
11000	2.961	2.628	2.390	2.205	2.056	3.538	3.270	3.061	2.962
12000	2.874	2.546	2.310	2.128	1.983	3.445	3.179	2.972	2.875
13000	2.796	2.471	2.238	2.060	1.917	3.360	3.097	2.890	2.795
14000	2.724	2.402	2.173	1.997	1.858	3.283	3.020	2.815	2.723
15000	2.658	2.339	2.113	1.940	1.804	3.210	2.950	2.745	2.657
16000	2.596	2.281	2.058	1.889	1.755	3.143	2.884	2.681	2.596
17000	2.539	2.227	2.007	1.841	1.710	3.081	2.823	2.621	2.539
18000	2.486	2.177	1.960	1.797	1.669	3.022	2.765	2.565	2.486
19000	2.436	2.131	1.916	1.756	1.630	2.967	2.712	2.513	2.436
20000	2.390	2.087	1.876	1.718	1.594	2.914	2.661	2.464	2.389
21000	2.345	2.046	1.837	1.682	1.561	2.865	2.613	2.418	2.346
22000	2.304	2.007	1.802	1.649	1.529	2.818	2.568	2.375	2.304
23000	2.265	1.971	1.768	1.617	1.499	2.774	2.526	2.335	2.265
24000	2.227	1.937	1.736	1.587	1.470	2.732	2.485	2.297	2.228
25000	2.192	1.904	1.706	1.559	1.443	2.692	2.447	2.261	2.193
30000	2.038	1.763	1.575	1.435	1.323	2.517	2.282	2.106	2.039
35000	1.913	1.650	1.469	1.333	1.223	2.375	2.150	1.983	1.914
40000	1.810	1.555	1.379	1.246	1.137	2.257	2.041	1.880	1.810
45000	1.721	1.473	1.301	1.169	1.061	2.157	1.948	1.792	1.721
50000	1.643	1.401	1.232	1.101	0.993	2.070	1.867	1.714	1.643
60000	1.513	1.279	1.113	0.984	0.877	1.925	1.729	1.578	1.511
70000	1.406	1.178	1.014	0.886	0.780	1.805	1.613	1.461	1.403
80000	1.315	1.091	0.929	0.802	0.699	1.703	1.511	1.358	1.310
90000	1.237	1.015	0.855	0.730	0.628	1.612	1.420	1.265	1.229
100000	1.167	0.948	0.790	0.666	0.567	1.531	1.338	1.180	1.156

TABLE 9. MEAN COLLISION INTEGRALS, $\sigma^2 \bar{\Omega}(i,j)$, FOR $N(^4S^0) - N(^4S^0)$ COLLISIONS

TEMP K	$\sigma^2 \bar{\Omega}(1,1)$	$\sigma^2 \bar{\Omega}(1,2)$	$\sigma^2 \bar{\Omega}(1,3)$	$\sigma^2 \bar{\Omega}(1,4)$	$\sigma^2 \bar{\Omega}(1,5)$	$\sigma^2 \bar{\Omega}(2,2)$	$\sigma^2 \bar{\Omega}(2,3)$	$\sigma^2 \bar{\Omega}(2,4)$	$\sigma^2 \bar{\Omega}(3,3)$
250	8.159	7.345	6.832	6.631	6.935	9.107	8.490	8.277	7.906
300	7.730	6.984	6.498	6.205	6.299	8.682	8.112	7.781	7.536
500	6.686	6.059	5.635	5.277	4.906	7.592	7.070	6.595	6.602
750	5.972	5.426	5.059	4.722	4.335	6.790	6.299	5.832	5.946
1000	5.523	5.032	4.697	4.395	4.098	6.269	5.818	5.415	5.522
2000	4.593	4.188	3.903	3.680	3.506	5.185	4.822	4.543	4.592
3000	4.121	3.752	3.496	3.303	3.149	4.637	4.316	4.078	4.111
4000	3.813	3.469	3.229	3.046	2.897	4.287	3.997	3.786	3.798
5000	3.588	3.259	3.027	2.847	2.696	4.040	3.774	3.580	3.569
6000	3.410	3.091	2.863	2.681	2.528	3.852	3.603	3.419	3.388
7000	3.264	2.951	2.723	2.540	2.386	3.702	3.464	3.285	3.238
8000	3.139	2.829	2.600	2.417	2.263	3.577	3.345	3.167	3.110
9000	3.030	2.721	2.492	2.309	2.157	3.469	3.240	3.061	2.998
10000	2.932	2.625	2.396	2.214	2.064	3.373	3.145	2.964	2.899
11000	2.844	2.538	2.310	2.129	1.982	3.286	3.059	2.875	2.810
12000	2.764	2.458	2.232	2.053	1.908	3.207	2.978	2.793	2.730
13000	2.691	2.386	2.161	1.984	1.842	3.134	2.904	2.718	2.656
14000	2.623	2.319	2.096	1.922	1.783	3.066	2.835	2.648	2.588
15000	2.561	2.258	2.036	1.865	1.728	3.002	2.771	2.583	2.525
16000	2.502	2.201	1.982	1.813	1.678	2.942	2.710	2.523	2.466
17000	2.447	2.148	1.931	1.765	1.633	2.886	2.654	2.467	2.411
18000	2.396	2.099	1.884	1.720	1.590	2.833	2.601	2.415	2.360
19000	2.348	2.052	1.840	1.678	1.551	2.783	2.551	2.366	2.311
20000	2.303	2.009	1.799	1.639	1.514	2.735	2.504	2.320	2.266
21000	2.260	1.968	1.760	1.603	1.480	2.690	2.459	2.277	2.223
22000	2.219	1.930	1.724	1.569	1.447	2.647	2.417	2.236	2.183
23000	2.181	1.893	1.690	1.537	1.417	2.606	2.377	2.197	2.145
24000	2.144	1.859	1.658	1.507	1.388	2.567	2.339	2.161	2.108
25000	2.109	1.826	1.627	1.478	1.361	2.530	2.303	2.126	2.074
30000	1.957	1.684	1.495	1.355	1.245	2.366	2.145	1.975	1.923
35000	1.833	1.570	1.390	1.256	1.152	2.232	2.016	1.852	1.802
40000	1.730	1.476	1.303	1.175	1.076	2.118	1.908	1.749	1.702
45000	1.642	1.396	1.229	1.107	1.012	2.021	1.816	1.661	1.616
50000	1.565	1.327	1.166	1.049	.958	1.935	1.735	1.583	1.542
60000	1.438	1.213	1.063	.954	.869	1.792	1.600	1.454	1.420
70000	1.337	1.123	.981	.878	.799	1.675	1.489	1.348	1.322
80000	1.253	1.049	.914	.816	.740	1.577	1.396	1.259	1.240
90000	1.183	.987	.858	.763	.690	1.493	1.317	1.183	1.169
100000	1.122	.934	.809	.717	.645	1.420	1.247	1.115	1.107

TABLE 10. MEAN COLLISION INTEGRALS, $\sigma^2 \bar{\Omega}(i,j)$, FOR $O^+(^4S^o) - O(^3P)$ COLLISIONS

TEMP K	$\sigma^2 \bar{\Omega}(1,1)$	$\sigma^2 \bar{\Omega}(1,2)$	$\sigma^2 \bar{\Omega}(1,3)$	$\sigma^2 \bar{\Omega}(1,4)$	$\sigma^2 \bar{\Omega}(1,5)$	$\sigma^2 \bar{\Omega}(2,2)$	$\sigma^2 \bar{\Omega}(2,3)$	$\sigma^2 \bar{\Omega}(2,4)$	$\sigma^2 \bar{\Omega}(3,3)$
250	3.416 (+1)	3.094 (+1)	2.938 (+1)	3.017 (+1)	3.139 (+1)	2.117 (+1)	1.805 (+1)	1.613 (+1)	3.049 (+1)
300	3.255 (+1)	2.991 (+1)	2.863 (+1)	2.867 (+1)	2.945 (+1)	1.910 (+1)	1.648 (+1)	1.485 (+1)	2.946 (+1)
500	2.943 (+1)	2.789 (+1)	2.704 (+1)	2.615 (+1)	2.519 (+1)	1.483 (+1)	1.315 (+1)	1.196 (+1)	2.732 (+1)
750	2.788 (+1)	2.679 (+1)	2.600 (+1)	2.486 (+1)	2.379 (+1)	1.250 (+1)	1.121 (+1)	1.020 (+1)	2.601 (+1)
1000	2.703 (+1)	2.606 (+1)	2.524 (+1)	2.423 (+1)	2.349 (+1)	1.118 (+1)	1.008 (+1)	9.230	2.519 (+1)
2000	2.513 (+1)	2.420 (+1)	2.351 (+1)	2.298 (+1)	2.263 (+1)	8.737	7.998	7.470	2.347 (+1)
3000	2.407 (+1)	2.324 (+1)	2.267 (+1)	2.226 (+1)	2.193 (+1)	7.651	7.017	6.535	2.266 (+1)
4000	2.339 (+1)	2.263 (+1)	2.211 (+1)	2.171 (+1)	2.138 (+1)	6.940	6.328	5.842	2.210 (+1)
5000	2.290 (+1)	2.218 (+1)	2.167 (+1)	2.127 (+1)	2.093 (+1)	6.396	5.786	5.299	2.167 (+1)
6000	2.251 (+1)	2.181 (+1)	2.131 (+1)	2.090 (+1)	2.054 (+1)	5.952	5.346	4.867	2.130 (+1)
7000	2.219 (+1)	2.150 (+1)	2.099 (+1)	2.057 (+1)	2.021 (+1)	5.581	4.982	4.518	2.099 (+1)
8000	2.192 (+1)	2.123 (+1)	2.071 (+1)	2.029 (+1)	1.992 (+1)	5.264	4.678	4.230	2.071 (+1)
9000	2.167 (+1)	2.098 (+1)	2.046 (+1)	2.003 (+1)	1.965 (+1)	4.991	4.420	3.990	2.046 (+1)
10000	2.145 (+1)	2.076 (+1)	2.023 (+1)	1.979 (+1)	1.940 (+1)	4.754	4.199	3.787	2.023 (+1)
11000	2.126 (+1)	2.056 (+1)	2.002 (+1)	1.957 (+1)	1.917 (+1)	4.545	4.007	3.613	2.002 (+1)
12000	2.107 (+1)	2.037 (+1)	1.982 (+1)	1.936 (+1)	1.895 (+1)	4.361	3.839	3.462	1.982 (+1)
13000	2.090 (+1)	2.019 (+1)	1.964 (+1)	1.917 (+1)	1.875 (+1)	4.196	3.691	3.329	1.964 (+1)
14000	2.074 (+1)	2.003 (+1)	1.946 (+1)	1.898 (+1)	1.856 (+1)	4.049	3.560	3.211	1.946 (+1)
15000	2.059 (+1)	1.987 (+1)	1.929 (+1)	1.881 (+1)	1.837 (+1)	3.916	3.442	3.105	1.930 (+1)
16000	2.045 (+1)	1.972 (+1)	1.914 (+1)	1.864 (+1)	1.820 (+1)	3.795	3.335	3.011	1.914 (+1)
17000	2.032 (+1)	1.958 (+1)	1.898 (+1)	1.848 (+1)	1.803 (+1)	3.685	3.238	2.925	1.899 (+1)
18000	2.019 (+1)	1.944 (+1)	1.884 (+1)	1.833 (+1)	1.787 (+1)	3.585	3.150	2.847	1.884 (+1)
19000	2.007 (+1)	1.931 (+1)	1.870 (+1)	1.818 (+1)	1.771 (+1)	3.492	3.070	2.775	1.870 (+1)
20000	1.995 (+1)	1.918 (+1)	1.857 (+1)	1.804 (+1)	1.757 (+1)	3.407	2.995	2.710	1.857 (+1)
21000	1.984 (+1)	1.906 (+1)	1.844 (+1)	1.790 (+1)	1.742 (+1)	3.327	2.927	2.649	1.844 (+1)
22000	1.973 (+1)	1.894 (+1)	1.831 (+1)	1.777 (+1)	1.728 (+1)	3.254	2.863	2.593	1.831 (+1)
23000	1.962 (+1)	1.883 (+1)	1.819 (+1)	1.764 (+1)	1.715 (+1)	3.185	2.804	2.541	1.819 (+1)
24000	1.952 (+1)	1.872 (+1)	1.807 (+1)	1.751 (+1)	1.702 (+1)	3.121	2.749	2.492	1.807 (+1)
25000	1.942 (+1)	1.861 (+1)	1.796 (+1)	1.739 (+1)	1.690 (+1)	3.061	2.697	2.446	1.796 (+1)
30000	1.897 (+1)	1.812 (+1)	1.743 (+1)	1.685 (+1)	1.635 (+1)	2.809	2.481	2.256	1.744 (+1)
35000	1.857 (+1)	1.769 (+1)	1.698 (+1)	1.639 (+1)	1.589 (+1)	2.615	2.316	2.111	1.699 (+1)
40000	1.821 (+1)	1.731 (+1)	1.659 (+1)	1.599 (+1)	1.550 (+1)	2.461	2.184	1.995	1.659 (+1)
45000	1.789 (+1)	1.697 (+1)	1.624 (+1)	1.565 (+1)	1.514 (+1)	2.335	2.077	1.900	1.624 (+1)
50000	1.760 (+1)	1.666 (+1)	1.593 (+1)	1.533 (+1)	1.481 (+1)	2.230	1.986	1.818	1.593 (+1)
60000	1.708 (+1)	1.612 (+1)	1.537 (+1)	1.474 (+1)	1.417 (+1)	2.061	1.839	1.683	1.538 (+1)
70000	1.663 (+1)	1.565 (+1)	1.487 (+1)	1.418 (+1)	1.352 (+1)	1.929	1.722	1.572	1.488 (+1)
80000	1.623 (+1)	1.522 (+1)	1.439 (+1)	1.361 (+1)	1.285 (+1)	1.821	1.623	1.475	1.441 (+1)
90000	1.587 (+1)	1.481 (+1)	1.391 (+1)	1.303 (+1)	1.216 (+1)	1.729	1.536	1.389	1.394 (+1)
100000	1.552 (+1)	1.441 (+1)	1.343 (+1)	1.245 (+1)	1.148 (+1)	1.648	1.458	1.310	1.347 (+1)

TABLE 11. MEAN COLLISION INTEGRALS, $\sigma^2 \bar{\Omega}(i,j)$, FOR $N^+(^3P) - N(^4S^o)$ COLLISIONS										
TEMP K	$\sigma^2 \bar{\Omega}(1,1)$	$\sigma^2 \bar{\Omega}(1,2)$	$\sigma^2 \bar{\Omega}(1,3)$	$\sigma^2 \bar{\Omega}(1,4)$	$\sigma^2 \bar{\Omega}(1,5)$	$\sigma^2 \bar{\Omega}(2,2)$	$\sigma^2 \bar{\Omega}(2,3)$	$\sigma^2 \bar{\Omega}(2,4)$	$\sigma^2 \bar{\Omega}(3,3)$	
250	4.185 (+1)	3.931 (+1)	3.767 (+1)	4.097 (+1)	4.247 (+1)	2.071 (+1)	1.891 (+1)	1.768 (+1)	3.781 (+1)	
300	4.051 (+1)	3.818 (+1)	3.669 (+1)	3.849 (+1)	4.512 (+1)	1.948 (+1)	1.788 (+1)	1.677 (+1)	3.683 (+1)	
500	3.737 (+1)	3.560 (+1)	3.444 (+1)	3.363 (+1)	6.896 (+1)	1.663 (+1)	1.537 (+1)	1.435 (+1)	3.454 (+1)	
750	3.547 (+1)	3.409 (+1)	3.306 (+1)	3.153 (+1)	6.393 (+1)	1.470 (+1)	1.354 (+1)	1.251 (+1)	3.309 (+1)	
1000	3.437 (+1)	3.315 (+1)	3.211 (+1)	3.069 (+1)	4.830 (+1)	1.340 (+1)	1.228 (+1)	1.132 (+1)	3.211 (+1)	
2000	3.184 (+1)	3.056 (+1)	2.952 (+1)	2.866 (+1)	2.925 (+1)	1.055 (+1)	9.614	8.926	2.952 (+1)	
3000	3.029 (+1)	2.902 (+1)	2.811 (+1)	2.742 (+1)	2.703 (+1)	9.172	8.401	7.857	2.812 (+1)	
4000	2.923 (+1)	2.803 (+1)	2.719 (+1)	2.656 (+1)	2.607 (+1)	8.344	7.664	7.163	2.721 (+1)	
5000	2.845 (+1)	2.730 (+1)	2.650 (+1)	2.588 (+1)	2.537 (+1)	7.754	7.102	6.587	2.652 (+1)	
6000	2.784 (+1)	2.673 (+1)	2.594 (+1)	2.533 (+1)	2.481 (+1)	7.278	6.619	6.072	2.596 (+1)	
7000	2.733 (+1)	2.625 (+1)	2.547 (+1)	2.485 (+1)	2.433 (+1)	6.866	6.187	5.612	2.548 (+1)	
8000	2.690 (+1)	2.583 (+1)	2.506 (+1)	2.443 (+1)	2.389 (+1)	6.498	5.797	5.205	2.507 (+1)	
9000	2.653 (+1)	2.547 (+1)	2.469 (+1)	2.405 (+1)	2.350 (+1)	6.164	5.446	4.847	2.469 (+1)	
10000	2.620 (+1)	2.514 (+1)	2.435 (+1)	2.371 (+1)	2.314 (+1)	5.859	5.130	4.531	2.436 (+1)	
11000	2.590 (+1)	2.484 (+1)	2.405 (+1)	2.339 (+1)	2.281 (+1)	5.580	4.846	4.252	2.405 (+1)	
12000	2.562 (+1)	2.456 (+1)	2.376 (+1)	2.309 (+1)	2.251 (+1)	5.324	4.589	4.004	2.376 (+1)	
13000	2.537 (+1)	2.430 (+1)	2.349 (+1)	2.282 (+1)	2.223 (+1)	5.089	4.358	3.784	2.349 (+1)	
14000	2.513 (+1)	2.406 (+1)	2.324 (+1)	2.256 (+1)	2.197 (+1)	4.873	4.148	3.588	2.324 (+1)	
15000	2.491 (+1)	2.384 (+1)	2.301 (+1)	2.232 (+1)	2.174 (+1)	4.674	3.957	3.411	2.301 (+1)	
16000	2.470 (+1)	2.362 (+1)	2.279 (+1)	2.210 (+1)	2.152 (+1)	4.490	3.783	3.253	2.279 (+1)	
17000	2.450 (+1)	2.342 (+1)	2.258 (+1)	2.190 (+1)	2.132 (+1)	4.320	3.625	3.109	2.258 (+1)	
18000	2.432 (+1)	2.323 (+1)	2.239 (+1)	2.171 (+1)	2.114 (+1)	4.163	3.480	2.979	2.239 (+1)	
19000	2.414 (+1)	2.305 (+1)	2.221 (+1)	2.153 (+1)	2.097 (+1)	4.016	3.346	2.861	2.221 (+1)	
20000	2.397 (+1)	2.288 (+1)	2.204 (+1)	2.136 (+1)	2.082 (+1)	3.880	3.224	2.754	2.204 (+1)	
21000	2.381 (+1)	2.271 (+1)	2.187 (+1)	2.121 (+1)	2.067 (+1)	3.753	3.111	2.655	2.188 (+1)	
22000	2.366 (+1)	2.256 (+1)	2.172 (+1)	2.106 (+1)	2.054 (+1)	3.635	3.007	2.565	2.172 (+1)	
23000	2.351 (+1)	2.241 (+1)	2.158 (+1)	2.093 (+1)	2.041 (+1)	3.525	2.910	2.482	2.158 (+1)	
24000	2.337 (+1)	2.227 (+1)	2.144 (+1)	2.080 (+1)	2.029 (+1)	3.421	2.821	2.406	2.144 (+1)	
25000	2.324 (+1)	2.213 (+1)	2.131 (+1)	2.068 (+1)	2.018 (+1)	3.324	2.737	2.336	2.131 (+1)	
30000	2.264 (+1)	2.155 (+1)	2.076 (+1)	2.016 (+1)	1.969 (+1)	2.920	2.398	2.053	2.076 (+1)	
35000	2.214 (+1)	2.107 (+1)	2.031 (+1)	1.974 (+1)	1.929 (+1)	2.615	2.150	1.851	2.031 (+1)	
40000	2.171 (+1)	2.067 (+1)	1.994 (+1)	1.939 (+1)	1.895 (+1)	2.380	1.963	1.700	1.994 (+1)	
45000	2.135 (+1)	2.033 (+1)	1.962 (+1)	1.908 (+1)	1.864 (+1)	2.193	1.816	1.582	1.962 (+1)	
50000	2.103 (+1)	2.003 (+1)	1.934 (+1)	1.881 (+1)	1.837 (+1)	2.041	1.699	1.487	1.934 (+1)	
60000	2.049 (+1)	1.953 (+1)	1.885 (+1)	1.832 (+1)	1.785 (+1)	1.811	1.521	1.342	1.885 (+1)	
70000	2.005 (+1)	1.911 (+1)	1.843 (+1)	1.787 (+1)	1.735 (+1)	1.644	1.392	1.233	1.843 (+1)	
80000	1.968 (+1)	1.874 (+1)	1.804 (+1)	1.743 (+1)	1.684 (+1)	1.517	1.291	1.146	1.804 (+1)	
90000	1.935 (+1)	1.840 (+1)	1.766 (+1)	1.699 (+1)	1.633 (+1)	1.415	1.209	1.073	1.766 (+1)	
100000	1.904 (+1)	1.808 (+1)	1.729 (+1)	1.655 (+1)	1.582 (+1)	1.331	1.139	1.010	1.729 (+1)	

states does not contribute to the collision integrals as heavily as the contributions from the high spin upper states. Secondly, although such extrapolations of the repulsive wall may introduce uncertainties in the cross sections at high energies, the effect on the collision integrals is diminished due to the factor e^{-x^2} in Eqn. (1).

Several collision integrals showing the interaction of oxygen atoms have been plotted in Figures 10, 11 and 12. The collision integrals $\sigma^2\overline{\Omega}(1,1)$ and $\sigma^2\overline{\Omega}(2,2)$ for the interaction of oxygen atoms in their ground state from Table 8 are shown in Figure 10. These curves are compared with our calculated results for interactions involving excited state atoms in Figures 11 and 12. Note that the results for the $O(^1S)-O(^1S)$ and $O(^1D)-O(^1S)$ states clearly exhibit the high temperature trend expected of excited states. Since atoms in the excited state are "bigger", i.e., the outer electrons are further away from the nucleus, one expects that the interaction energy is larger and $\sigma^2\overline{\Omega}$ would increase with excitation energy. However, Figures 11 and 12 show that the values of $\sigma^2\overline{\Omega}$ for other excited state interactions do not all follow this trend. Part of this behavior is explained by the tendency of the repulsive wall of the potential curve to be pushed to smaller R by curve crossing interactions. This results in smaller values of the collision integrals. Note also that the collision integrals of the $O(^1S)-O(^1S)$ interaction are small at low temperatures. This is expected because of the repulsive non-bonding nature of the interaction at large separation distances.

We conclude our discussion of the results by displaying some plots of transport quantities that may be obtained readily from the tabulated values of the collision integrals. The viscosity for a gas of oxygen atoms in their ground states is shown in Figure 13. As can be seen by comparing Tables 8 and 9, the corresponding values for nitrogen are very close to these results. The thermal conductivity and self-diffusion coefficient of these two gases are compared in Figures 14 and 15, respectively. The binary diffusion coefficient for an N^+-N mixture and for an O^+-O mixture are also shown in Figure 15. Note that the ion-atom curves lie considerably above the atom-atom curves; this is due to the fact that resonance charge exchange is an important mechanism for charge diffusion. The transport quantities shown in Figures 13-15 can be used as input for the determination of transport properties of mixtures such as that occurring in high temperature air.

VI. CONCLUDING REMARKS

We have developed a general method to permit a direct determination of transport collision cross sections from discrete potential data, rather than less reliable fits to analytical potential functions. Our semiclassical methods account for quantum mechanical effects such as resonance charge exchange, which is important at high temperatures, without the use of ad-hoc assumptions. The code can accomodate the case of multiple turning points; e.g., when the potential energy exhibits barriers which can arise from the non-crossing of potential curves for states of like symmetry (avoided crossings).

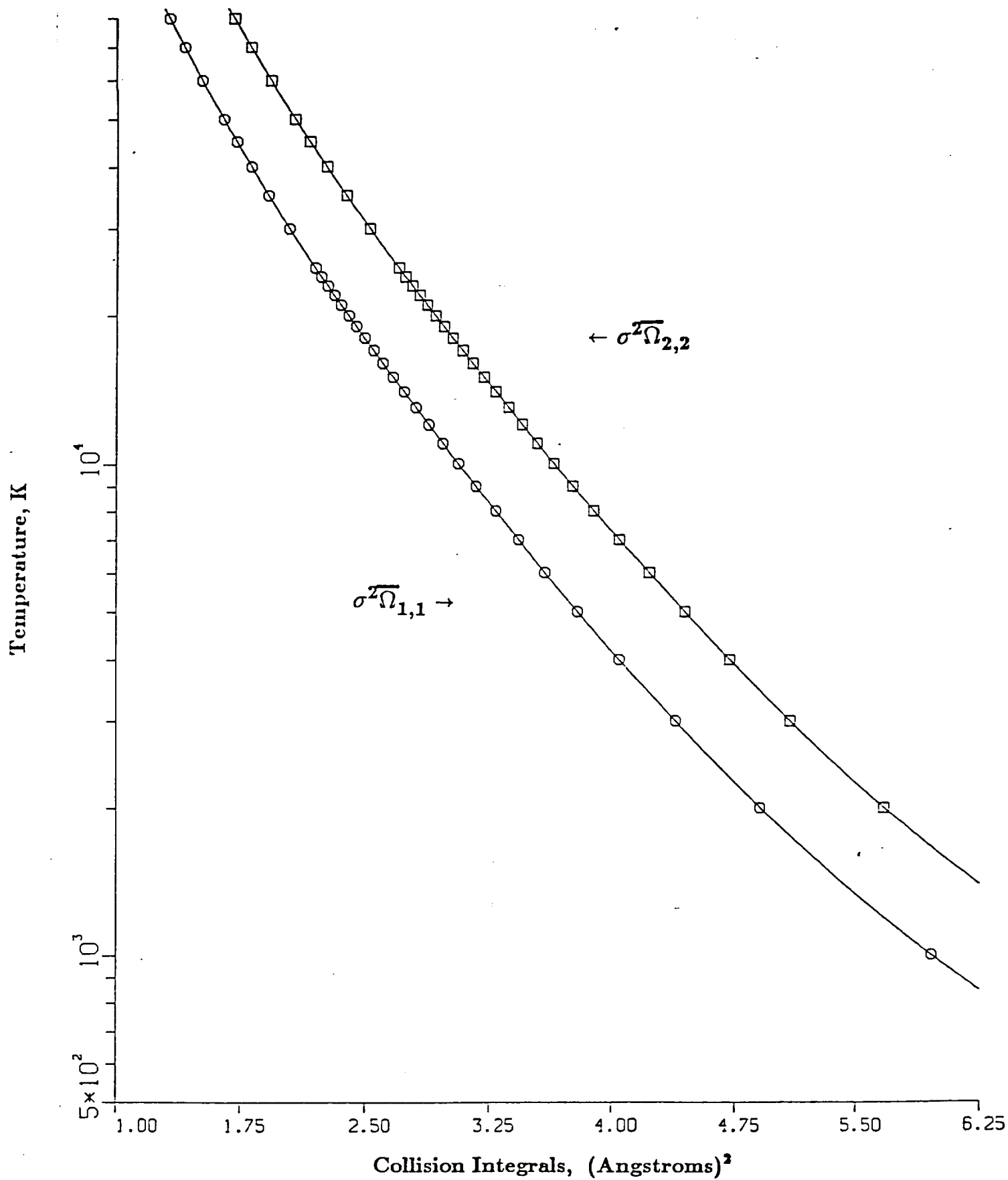


Figure 10. Collision Integrals for Ground State, O(³P)–O(³P)

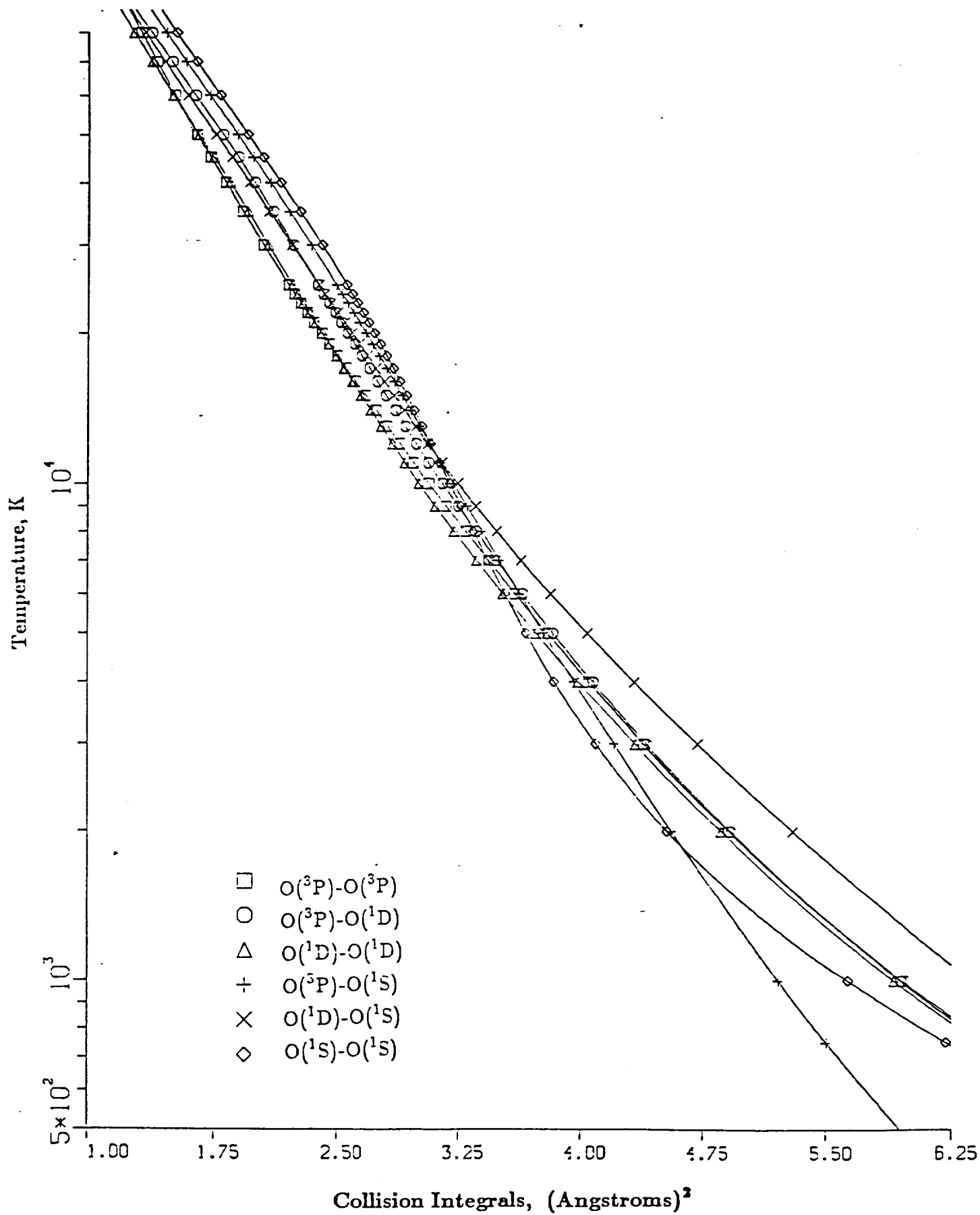


Figure 11. Collision Integrals $\sigma^2 \bar{n}_{1,1}$ for O-O Interactions

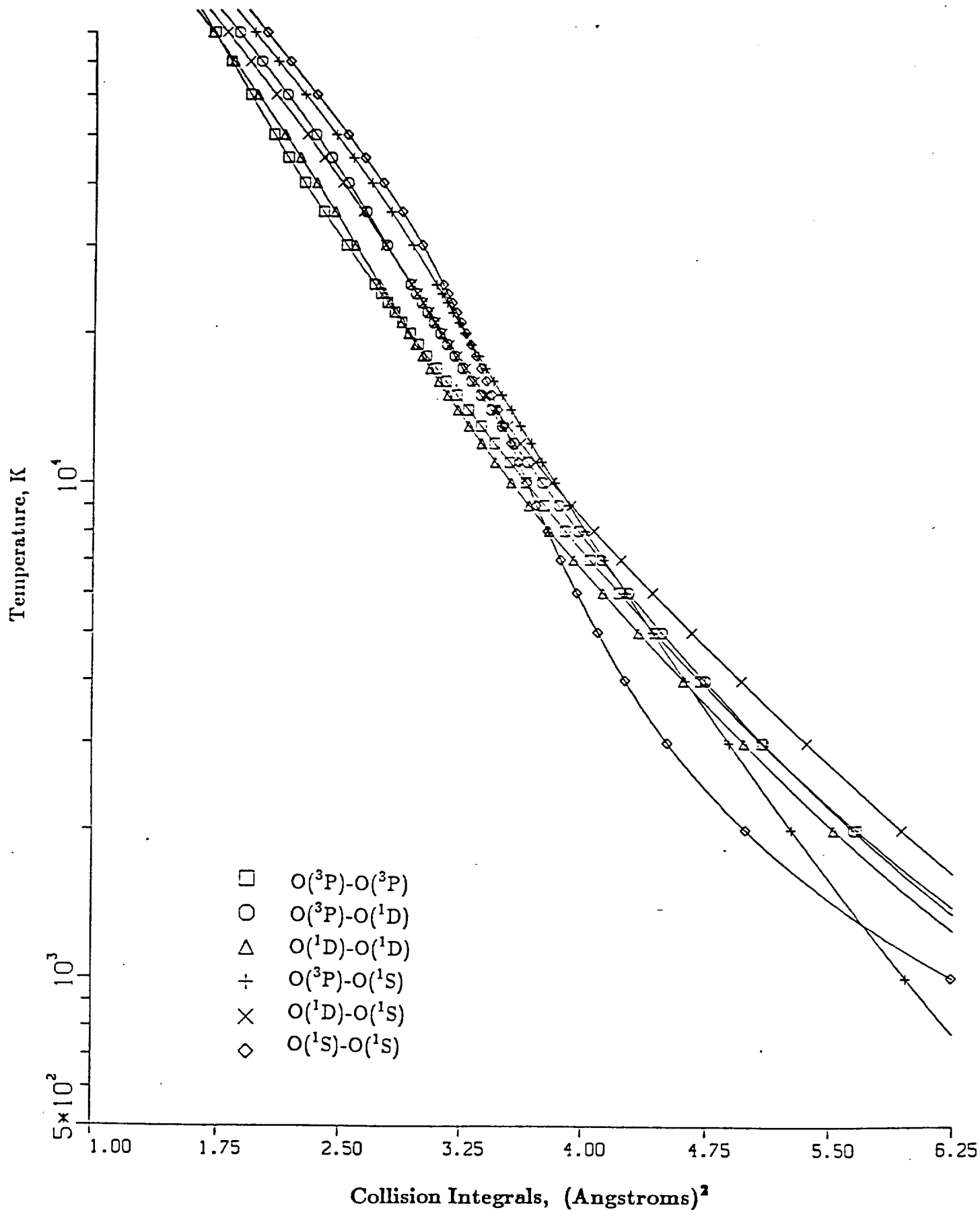


Figure 12. Collision Integrals $\sigma^2 \bar{n}_{2,2}$ for O-O Interactions

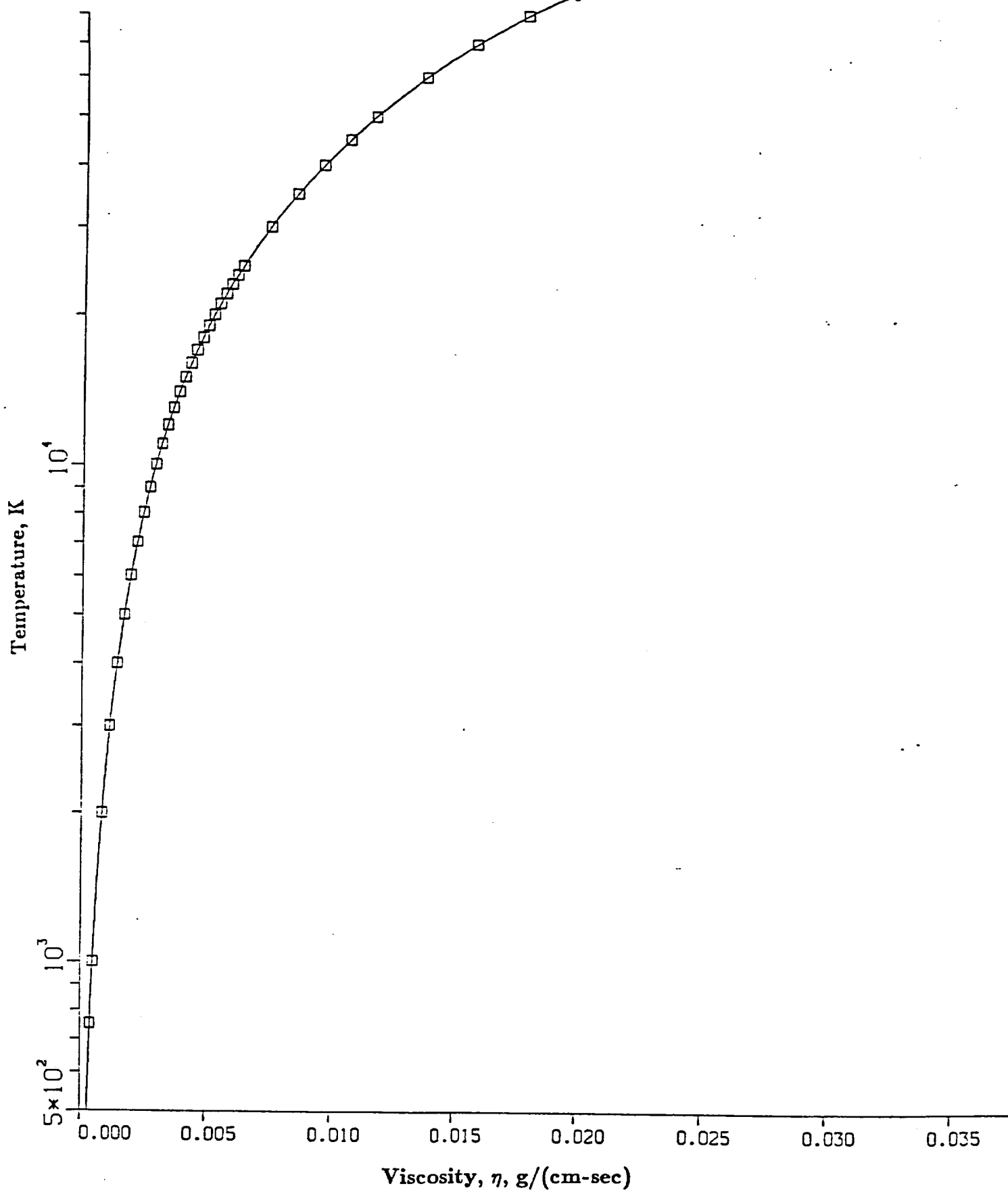


Figure 13. Viscosity for a Gas of Ground State Oxygen Atoms

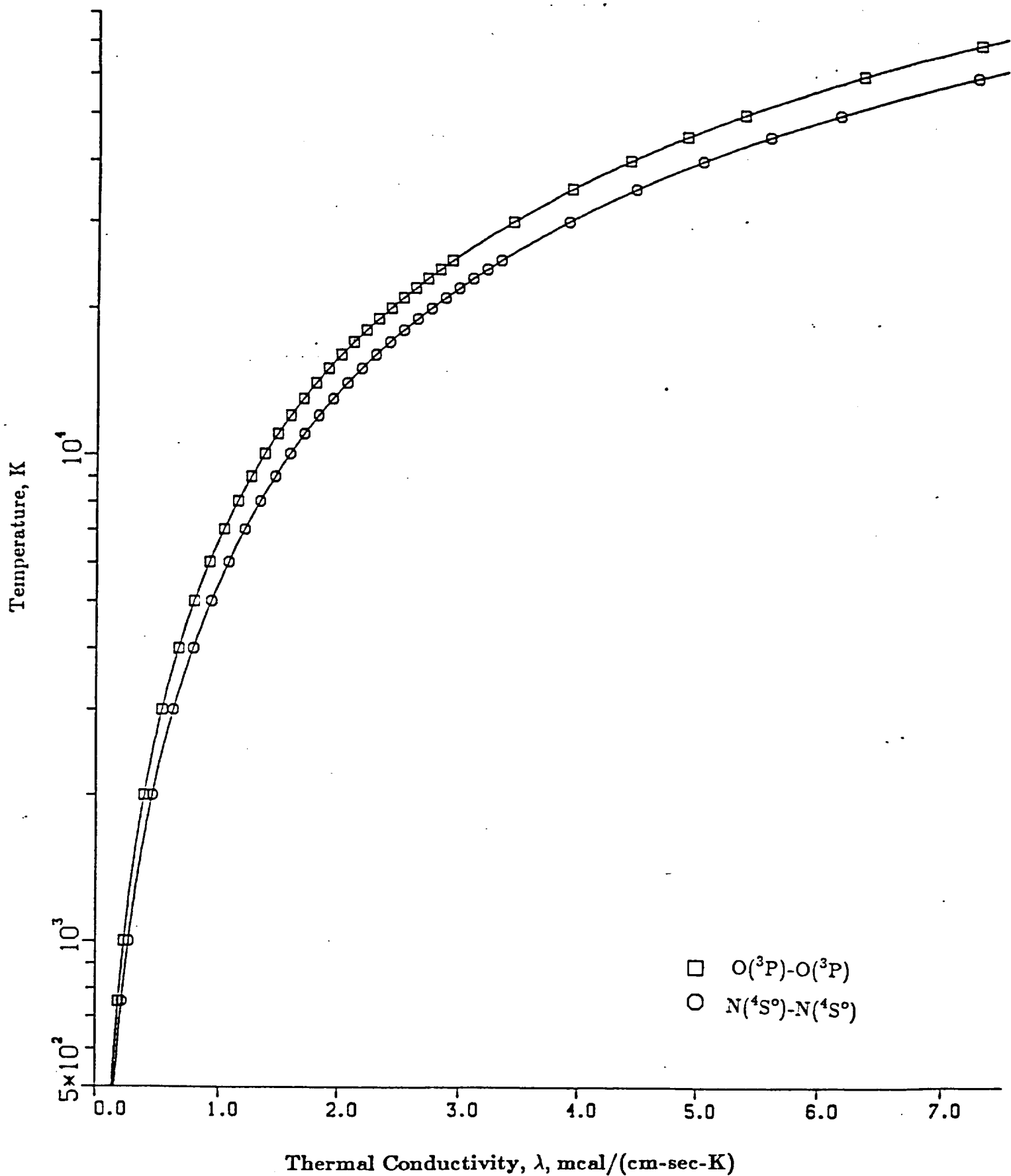


Figure 14. Thermal Conductivities for Oxygen and Nitrogen

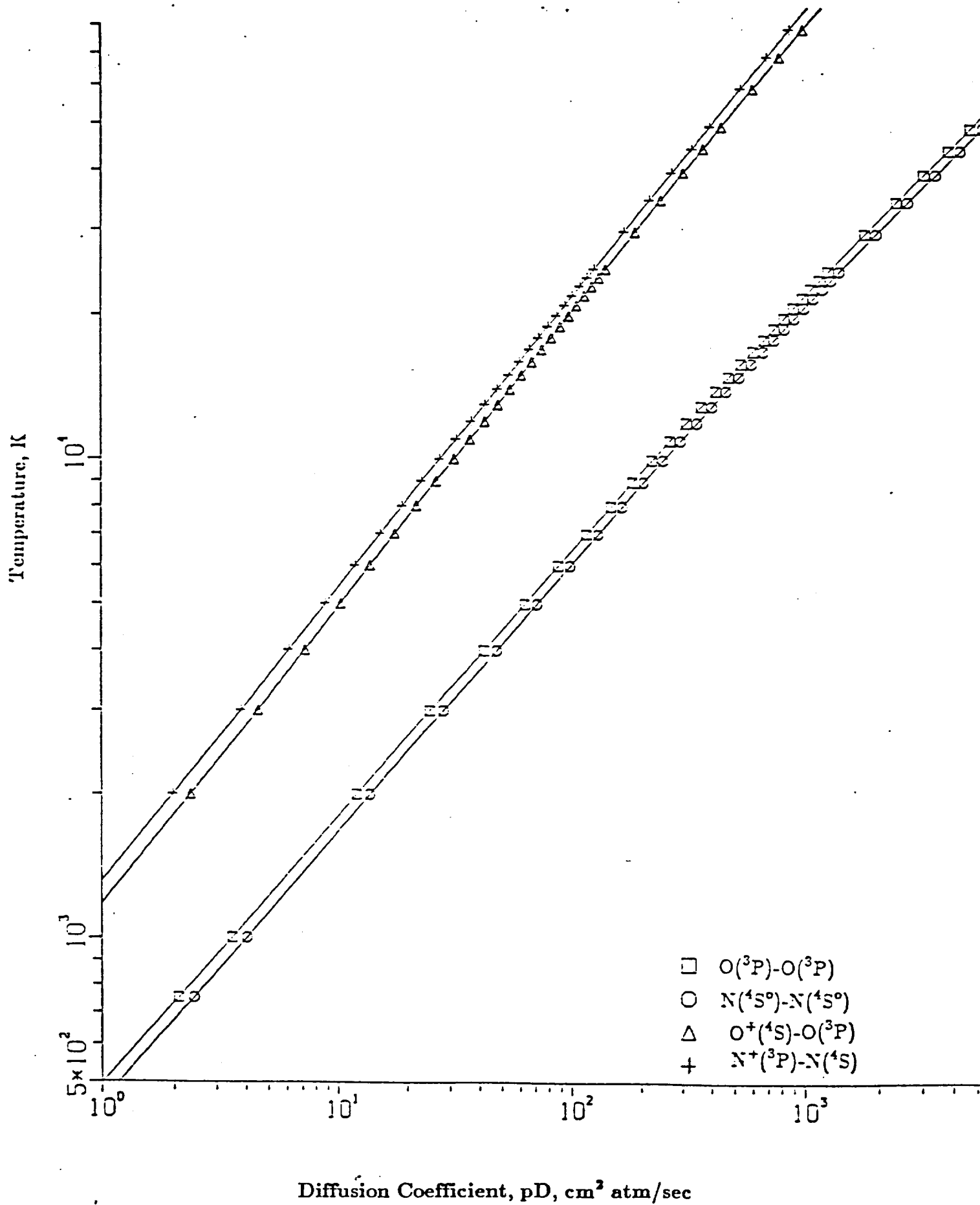


Figure 15. Diffusion Coefficients for Oxygen and Nitrogen